

Effect of End-of-Life (EOL) Content in High-Vacuum High-Pressure Die Cast
(HVHPDC) A365-T7 on Corrosion Behaviour

Effect of End-of-Life (EOL) Content in High-Vacuum High-Pressure Die Cast
(HVHPDC) A365-T7 on Corrosion Behaviour

By YUKI ANDO, B.ENG.

A Thesis

Submitted to the Department of Materials Science & Engineering and the School of
Graduate Studies

in Partial Fulfilment of the Requirements for the Degree
Master of Applied Science

McMaster University

© Copyright by Yuki Ando, April 2023

McMaster University

Hamilton, Ontario

MASTER OF APPLIED SCIENCE (2023)

(Materials Science & Engineering)

TITLE:

Effect of End-of-Life (EOL) Content in High-Vacuum High-Pressure Die Cast (HVHPDC) A365-T7 on Corrosion Behaviour

AUTHOR:

Yuki Ando B. Eng. (McMaster University)

SUPERVISOR:

Dr. J.R. Kish and Dr. S. Shankar

NUMBER OF PAGES:

93

Abstract

The recent awareness of global warming and climate change has triggered the idea of implementing End-of-Life (EOL) materials to fabricate secondary cast Al alloys; this is to further consider more sustainable manufacturing, which is also expected to reduce the greenhouse gas (GHG) emission of automotive component manufacturing.

In this research, the effect of EOL materials implemented in high-vacuum high-pressure die cast (HVHPDC) A365-T7 alloy on corrosion behaviour was investigated. A365-T7 alloys with different EOL contents (0%, 40%, 75%, and 90%) were fabricated by Nematik Monterrey. The chemical composition of primary alloy and secondary alloys was comparable except for impurity elements such as Cu and Zn, and lower Ti content were observed in the secondary alloy. Corrosion experiments indicated that all secondary alloys were more susceptible to localized corrosion initiation, and the effect of EOL content in secondary alloys was found to be minor. Microstructure characterization revealed several features; the primary Al cell size of primary alloy at the skin region was smaller than ones observed in secondary alloys. Smaller fraction of Fe-containing intermetallic particles (IMPs) was also observed in the primary alloy. Passive film investigation was conducted on EOL 0 and EOL 40 (representing secondary alloys); Mg and Zn were detected on the passive film of EOL 40. Three working theories on localized corrosion initiation susceptibility were established: (i) effect of Fe-containing IMPs, (ii) effect of structure refinement (iii), and effect of Mg and Zn on the passive film. It was concluded that the localized corrosion initiation susceptibility of secondary alloy may be influenced by one or a combination of those working theories.

This research investigated the effect of EOL materials on corrosion behaviour which is one of the most essential properties of cast Al alloys. Successful understanding of such effects would enhance the utilization of EOL materials.

Acknowledgement

First, I would like to thank my supervisors, Dr. Joey Kish, and Dr. Sumanth Shankar for providing me with a motivating project and continuous support during my master's studies. I also deeply appreciate that they allowed me to attend many conferences and visit facilities to enhance my academic and professional experiences. I truly believe that my master's study experience would have not been this pleasant without them. I am very grateful to have them as my supervisors.

I would also like to thank the engineering team from Nematik USA/Canada and Nematik Monterrey, Dr. Glenn Byczynski, Dr. Anthony Lombardi, and Dr. Alejandro Gonzalez. They have been always involved with my project through bi-weekly meetings and provided numerous pieces of advice. I truly believe that I would have not been able to learn this much without their support and kindness. I would also like to thank Dr. Alejandro Gonzalez and his team members at Nematik Monterrey for their support during my facility visit in Monterrey, Mexico.

Many thanks go to members of the Center for Automotive Materials and Corrosion, as well as staff at the Centre of Canadian Electron Microscopy. I would like to thank Dr. Joe McDermid for providing support and discussion regarding my project. He certainly spent time to provide guidance and advice to maximize my master's study experience. I would like to show my appreciation to Dr. Beth McNally who provided many in-lab trainings and support, as well as personal caring that she provided me during my master's study. I would also like to appreciate Chris Butcher and Jhoynner Martinez for their support with scanning electron microscopy operations. Finally, I would like to

acknowledge Dr. Zeynel Bayindir from Biointerfaces institute at McMaster University for the X-ray photoelectron spectrometer operations.

I would like to thank all graduate students in Dr. Joey Kish's research group and the colleagues in the Department of Materials Science and Engineering. Special thank you to Sara Filice, who has been always providing her true support to my entire master's study. I would like to deeply appreciate what she has done during my master's study.

I would also like to thank my personal friends: Youssef Salib, Karim Salib, Abdullah Wasseem, Ibrahim Wasseem, Hamza Wasseem, Sean Khoi, Santiago Parra, and Talha Aziz. Their supports during my master's study were truly a huge part of my successful master's study.

Lastly, I would like to thank my parents and siblings for their continuous support. Ever since I left my home country when I was fifteen years old, there was not a single time that they did not provide me with support and all the cheering that I could asked for. The support and care that I receive from my family are unparalleled, and I would not be the person that I am at this stage without them.

List of Abbreviations

AA	Aluminum Association
BSE	Backscatter Electron
EDS	Energy-dispersive X-ray Spectroscopy
EOL	End-of-Life
GHG	Greenhouse Gas
GP	Guinier-Preston
HPDC	High-Pressure Die Cast
HVHPDC	High-Vacuum High-Pressure Die Cast
ICP-MS	Inductively Coupled Plasma – Mass Spectroscopy
IMP	Intermetallic Particle
LOM	Light Optical Microscopy
OCP	Open Circuit Potential
OEM	Operation Equipment Manufacturer
PM	Permeant Mold
SE	Secondary Electron
SEM	Scanning Electron Microscopy
SKPFM	Scanning Kelvin Probe Force Microscopy
SSSS	Supersaturated Solid Solution
TEM	Transmission Electron Microscopy
TT	Through-Thickness
XPS	X-ray Photoelectron Spectroscopy
XRD	X-Ray Diffraction

List of Symbols

°C	Celsius degree
%	Percent
cm ²	Centimetre square
E _b	Breakdown Potential
E _r	Repassivation Potential
h	Hour
Hz	Hertz
keV	Kilo electron-volt
mA	Milliampere
MPa	Megapascal
mV	Millivolt
W	Watt
Wt%	Weight percentage

Table of Contents

Abstract	iv
Acknowledgement	vi
List of Abbreviations	viii
List of Symbols	ix
Table of Contents	x
Table of Tables	xii
Table of Figures	xiv
Chapter 1: Introduction	1
Chapter 2: Literature Review	5
2.1: Aluminum Alloy	5
2.2 High Pressure Die Casting (HPDC)	7
2.3 Heat Treatment and Microstructure of Al Alloy Castings.....	10
2.4 Localized Corrosion of Hypoeutectic Al-Si Alloy Castings	18
2.4.1 Cyclic potentiodynamic anodic polarization.....	18
2.4.2 Passive film breakdown	21
2.4.3 Localized corrosion initiation	22
2.4.4 Localized corrosion propagation.....	25
2.5 Secondary Hypoeutectic Al-Si-Mg Alloy Castings.....	26
2.5.1 Mechanical properties of cast secondary Al-Si-Mg alloy.....	27
2.5.2 Corrosion behaviour of cast secondary Al-Si-Mg alloys.....	30
Chapter 3: Research Objective.....	33
Chapter 4: Experimental Procedure	35
4.1 Materials	35
4.2 Microstructure Characterization	36
4.3 Corrosion Experiments	39
4.3.1 Electrochemical Polarization	39
4.3.2 Corrosion Visualization	41
4.3 X-Ray Photoelectron Spectroscopy (XPS).....	42
Chapter 5: Results	44
5.1 Starting Microstructure Characterization	44
5.2 Electrochemical Polarization Measurements.....	51
5.3 Corrosion Visualization Experiment	59
5.4 X-Ray Photoelectron Spectroscopy.....	61

Chapter 6: Discussion	66
Chapter 7: Conclusion and Future Work	72
Appendix	75
Reference	82

Table of Tables

Table 2.1: Identification system for Al alloy castings based on principal alloying elements [20].....	5
Table 2.2: Alloying element and composition limit (wt%) of A 365 [21]	5
Table 2.3: Purpose and effect of main alloying elements in A365	6
Table 2.4: Temper designation and description specified for Al alloys [19].....	11
Table 2.5: Precipitation sequence and solidification temperature of Fe-bearing IMPs [39]	17
Table 2.6: Qualitative effect of Fe-bearing IMPs on mechanical properties of hypoeutectic Al-Si alloy castings [42]	18
Table 2.7: Potential differences relative to primary Al phase, measured by SKPFM on A356 [8]	23
Table 2.8: EDS point analysis on eutectic phase and IMPs [63]	26
Table 2.9: Chemical composition of developed secondary A 365 alloys (Fe Enrichment Factor = Fe content of secondary / Fe content of primary alloy (=0.2)).....	29
Table 2.10: Mechanical properties of secondary alloy investigated by Cinkilic et al. [15]	29
Table 2.11: Chemical composition of investigated secondary A 365 alloy (Fe Enrichment Factor = Fe content of secondary / Fe content of primary alloy (=0.2)).....	31
Table 4.1: Chemical composition of EOL alloys, obtained by ICP-MS analysis (wt%)...35	35
Table 5.1: Primary Al phase cell size in the four EOL alloys	46
Table 5.2: Microstructure characteristics obtained by SEM-BSE images.....	48
Table 5.3: Elemental composition of spot analysis (wt%)	50
Table 5.4: Elemental composition of spot analysis (wt%)	51
Table 5.5: Average values of breakdown potential (E_b), repassivation potential (E_r), and ΔV ($E_b - E_r$) with 95% confidence intervals, skin region	52
Table 5.6: Average values of breakdown potential (E_b), repassivation potential (E_r), and ΔV ($E_b - E_r$) with 95% confidence intervals, core region.....	53

Table 6.1: Electrochemical characteristics of EOL 0 and EOL 40.....	67
Table 6.2: Microstructure characteristic of EOL 0 and EOL 40 (skin region).....	67
Table 7.1: Future work regarding the proposed working theories.....	74

Table of Figures

Figure 1.1: Cross sectional light optical microscopy (LOM) images of localized corrosion attack, captured by Nematik [19]	3
Figure 2.2: Al-Si phase diagram [28]	7
Figure 2.3: LOM image of the microstructure of HPDC (a-c) and PM (e-f) AlMg ₅ Si ₂ Mn, A: Large primary Al phase, B: small primary Al phase, region C: α -Al ₁₅ (Mn, Fe) ₃ Si ₂ , D: β -Al ₅ FeSi [2].....	8
Figure 2.4: Schematic illustration of the HVHPDC process, (a): prior to molten metal injection (b): vacuum valve activated while molten metal is injected into the cavity [31] .	9
Figure 2.5: Variation of yield strength and elongation of Al alloy A365.0 with various heat treatments applied [21].....	12
Figure 2.6: SEM microstructure images of A 365 alloy, (a): As-cast (b) T6 heat treatment [6].....	12
Figure 2.7: TEM images of α' -Mg ₂ Si and β'' -Mg ₂ Si precipitates with various solutionizing time (at 540 °C) and artificial aging time (at 175 °C) [40].....	15
Figure 2.8: Phase diagram of Al-Fe system [41], showing the low eutectic composition of Fe in Al (\cong 0.05 wt%)	16
Figure 2.9: Microstructure images showing morphology of (a): β -Al ₅ FeSi, (b): α -Al ₁₅ (Fe,Mn) ₃ Si ₂ [13]	17
Figure 2.10: Illustration of cyclic polarization measurement behaviour, (a): with repassivation potential, (b) oxygen evolution, and (c) without repassivation potential [47]	19
Figure 2.11: Cyclic polarization schematic with description of stable localized corrosion initiation and propagation [47].....	20
Figure 2.12: SEM images of AlSi8Mg14 alloy (a): before the NaCl solution immersion, (b): after the NaCl solution immersion [60]	23

Figure 2.13: Potentiodynamic polarization curve of AlFe_3 and $\alpha\text{-Al}(\text{Mn,Fe})\text{Si}$ with 0.1 M $\text{Na}(\text{OH})$ solution, indicating the lower anodic and cathodic current density observed on $\alpha\text{-Al}(\text{Mn,Fe})\text{Si}$ [61]	24
Figure 2.14: (a) LOM image of cross section of post corrosion test (b) SEM image of corrosion site (after potentiodynamic anodic polarization with 0.5 M NaCl solution) [63]	25
Figure 2.15: Phase fraction of $\alpha\text{-Al}_{15}(\text{Fe,Mn})_3\text{Si}_2$ and $\beta\text{-Al}_5\text{FeSi}$ as a function of Mn content. The model is $\text{AlSi}10.5\text{Mg}0.4\text{Fe}0.55\text{-Mn}$ at equilibrium condition. Segregation factor = $\text{Fe} + 2\text{Mn} + 3\text{Cr}$ [13]	28
Figure 2.16: LOM images of cross section of post corrosion test, (a): skin region (b): core region of secondary A359 alloys (cyclic polarization with 0.05M NaCl solution) [18] ...	32
Figure 4.1: SEM-backscatter electron (BSE) image of EOL 0, describing the direction orientation of the cast.....	36
Figure 4.2: Imaging process of primary Al cell size measurement, (a): 8-bit image (b): processed image revealing Al dendrite (c): linear interception for cell size measurement, thick red line indicating the primary Al cell size	38
Figure 5.1: Microstructure images of each EOL alloy obtained by LOM, cross section view. Red dotted lines demark the interface between the skin (located on either side) and the core.....	44
Figure 5.2: Cross sectional microstructure images of each EOL alloy: (a) skin and (b) core.....	45
Figure 5.3: BSE images of each EOL alloy, skin region	46
Figure 5.4: BSE images of each EOL alloy, core region.....	47
Figure 5.5: EDS mapping of EOL 0, skin region	50
Figure 5.6: EDS mapping of EOL 40, skin region	51
Figure 5.7: Representative cyclic polarization curves of each EOL alloy, skin region.....	52
Figure 5.8: Representative cyclic polarization curves of each EOL alloy, core region.....	53
Figure 5.9: Cross sectional images of post potentiostatic anodic polarization, obtained by LOM, polarization measurement conducted by Darren Feenstra	55

Figure 5.10: Potential transient of each EOL alloy during galvanostatic anodic polarization (+ 1 mA/cm ² for 5 h).....	56
Figure 5.11: Cross sectional images of post galvanostatic anodic polarization	57
Figure 5.12: Current density transients of EOL 0 and EOL 40 with an applied metastable potential (20 mV below E _b)	58
Figure 5.13: Images of agar gel electrolytes at the beginning of the experiment (0 h)	60
Figure 5.14: Images of agar gel electrolytes after 4 h of the exposure, dotted line demarks the cathodic region (blue colour)	61
Figure 5.15: Concentration depth profile for O as a function for sputter time, EOL 0 and EOL 40; Solid lines demark the passive film/metal interface.	63
Figure 5.16: Atomic concentration of detected element as a function of sputter time during depth profiling, EOL 0 and EOL 40. Dotted line indicating passive film/metal interface of each EOL alloy	65
Figure 6.1: Illustration of the effect of Mg-rich zone on the passive film stability [78]	71
Figure A.1: Replicate dataset of cyclic potentiodynamic polarization, skin region, EOL 0	75
Figure A.2: Replicate dataset of cyclic potentiodynamic polarization, skin region, EOL 40	75
Figure A.3: Replicate dataset of cyclic potentiodynamic polarization, skin region, EOL 75	76
Figure A.4: Replicate dataset of cyclic potentiodynamic polarization, skin region, EOL 90	76
Figure A.5: Replicate dataset of cyclic potentiodynamic polarization, core region, EOL 0	77
Figure A.6: Replicate dataset of cyclic potentiodynamic polarization, core region, EOL 40	77
Figure A.7: Replicate dataset of cyclic potentiodynamic polarization, core region, EOL 75	78

Figure A.8: Replicate dataset of cyclic potentiodynamic polarization, core region, EOL 90	78
Figure A.9: Replicate dataset of galvanostatic polarization, EOL 0.....	79
Figure A.10: Replicate dataset of galvanostatic polarization, EOL 40.....	79
Figure A.11: Replicate dataset of galvanostatic polarization, EOL 75.....	80
Figure A.12: Replicate dataset of galvanostatic polarization, EOL 90.....	80
Figure A.13: Replicate dataset of current density transient for metastable localized corrosion initiation, EOL 0	81
Figure A.14: Replicate dataset of current density transient for metastable localized corrosion initiation, EOL 40	81

Chapter 1: Introduction

Aluminum (Al) alloys are used widely in many applications such as structural, automotive, aerospace, and space industries. Their strength-to-weight ratio can be substantially high, depending on the alloying elements and post treatment. Cast Al alloys are especially advantageous for the purpose of large mass productions; for instance, components with complex geometries can be fabricated without any post-machining processes. Cast Al alloy 3xx.x series have an excellent balance of adequate mechanical properties and corrosion resistance, which are commonly adopted for some automotive components such as engine blocks, shock tower, and chassis parts [1] [2] [3]. Use of cast Al alloys in automotive application offers many other advantages, including the expectation to reduce the greenhouse gas (GHG) emission by lightweighting the automotive components. An increase in the awareness of global warming and climate change has triggered to further emphasize on reducing GHG emission. One viable approach for this objective is to utilize recycled End-of-Life (EOL) materials [4]. EOL materials include Al alloy components that reached their lifespan and scrap Al from Al alloy manufacturing. Fabrication of cast Al alloys with EOL materials, known as secondary alloy, can reduce the electricity consumption by 90 - 95% compared to primary alloy [5], depending on the amount of EOL materials introduced.

The microstructure of cast Al alloy 3xx.x series (Al-Si) consists of Al-matrix, Si eutectic phase, intermetallic particles (IMPs), and strengthening precipitates induced by heat treatment [6]. The localized corrosion mechanism of cast Al-Si alloys is fairly

established, whereby Si eutectic phase being more noble than primary Al phase, induces micro-galvanic corrosion between those two phases [7]. However, it is known that the presence of Si eutectic phase also does not solely promote localized corrosion. Fe-containing IMPs such as β -Al₃FeSi, α -Al₈Fe₂Si, and α -Al₁₅(Fe,Mn)₃Si₂ are more noble than Si eutectic [8], leading to a severe galvanic effect between primary Al phase and IMPs [9]. Ultimately, the presence of Fe-containing IMPs increases localized corrosion susceptibility of cast Al-Si alloys.

One of the challenges associated with an implementation of EOL materials is impurity elements control. These impurity elements such as Fe, Cu, and Zn, affect the microstructure of cast Al alloys, thus influencing the mechanical and corrosion properties of secondary alloys [10] [11] [12]. Controlling the Fe content with the utilization of EOL materials is difficult and has been investigated. In contrast, recent research has established that the mechanical properties of secondary cast Al-Si alloys are comparable to primary alloy with the modification of chemical composition and heat treatment [13] [14] [15]. Yet, there is a lack of understanding on the localized corrosion susceptibility and corrosion behaviour of secondary cast Al-Si alloys.

Secondary cast Al-Si alloys that were previously investigated contain a higher amount of Fe in comparison to the primary alloy which leads to having more Fe-containing IMPs within the cast [16]. Consequently, it is apparent that the increased fraction of Fe-containing IMPs results in a detrimental effect on the corrosion resistance of secondary alloys [17] [18]. Nematik has developed an EOL blending strategy for high vacuum high pressure die casting (HVHPDC) process that can maintain the Fe content in secondary

A365-T7 alloys comparable to that of the primary alloy. However, only the primary alloy passed the original equipment manufacturer (OEM)'s internal acceptance criterion for corrosion resistance. In other words, corrosion resistance was still compromised despite the controlled Fe content, as shown in Figure 1.1. This demonstrates a lack of understanding in corrosion behaviour of secondary A365-T7 alloys.

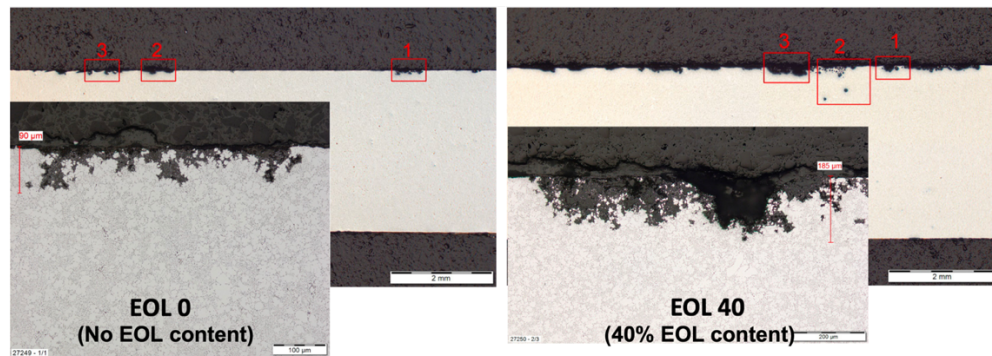


Figure 1.1: Cross sectional light optical microscopy (LOM) images of localized corrosion attack, captured by Nemak [19]

The purpose of this research is to determine the localized corrosion susceptibility of secondary A365-T7 (Aural™-2, AlSi10MnMg-T7), near net shaped castings produced by HVHPDC using different EOL contents. Localized corrosion susceptibility was evaluated in terms of initiation and propagation using electrochemical polarization and corrosion visualization techniques coupled with post-exposure examination using LOM and scanning electron microscopy (SEM). A complementary analysis of the surface films formed during anodic oxidation was also conducted using X-ray photoelectron spectroscopy (XPS). Identifying of the critical factor(s) that drive localized corrosion initiation and propagation is required to further develop the blending strategy to one that

produces secondary alloys that will consistently meet various OEM's internal corrosion performance acceptance requirements.

Chapter 2: Literature Review

2.1: Aluminum Alloy

The addition of certain elements, including Si, Mg, Cu, and Zn, can significantly impact the strength of Al and its alloys. A standardized system for designating Al alloys based on the alloying elements has been established by the Aluminum Association (AA).

Table 2.1 summarizes this identification system for Al alloy castings.

Table 2.1: Identification system for Al alloy castings based on principal alloying elements [20]

Principal Alloying Elements	Designation Series
Pure Aluminum	1xx.x
Copper	2xx.x
Silicon + Magnesium (+ Copper)	3xx.x
Silicon	4xx.x
Magnesium	5xx.x
Zinc	7xx.x

The first digit indicates the principal alloying element. The second and third digits indicate other specific alloying elements. The decimal indicates the product form, typically casting or ingot [21]. 2xx.x, 3xx.x, and 7xx.x series are heat-treatable Al alloys, whereas the others are non-heat-treatable. This research focused on the localized corrosion susceptibility of primary and secondary hypoeutectic Al-Si alloy A365; the major alloying elements of which were Si, Mg, Mn, Ti and specified amount of Fe, as shown in Table 2.2.

Table 2.2: Alloying element and composition limit (wt%) of A 365 [21]

Si	Mg	Mn	Ti	Fe	Zn
9.5 – 11.5	0.1 – 0.5	0.5 – 0.8	0.04 – 0.15	0.15 – 0.25	0.03 max

The alloying elements in A 365 alloy casting and their purposes are summarized in Table 2.3.

Table 2.3: Purpose and effect of main alloying elements in A365

Alloying Element	Purpose
Si	Main alloying element that increases the fluidity of molten Al [22]. Improved mechanical properties due to Al-Si eutectic phase [23], as well as cooperate with Mg to form strengthening precipitates during post-casting heat treatment.
Mg	Forming Mg ₂ Si strengthening precipitates to improve overall mechanical properties during post-casting heat treatment [24].
Fe	Avoiding die soldering to obtain proper surface finishing of the casting [25].
Mn	Altering the morphology and chemistry of Fe-containing IMPs such as β -Al ₃ FeSi [26]. Avoiding die soldering phenomena when Fe content is low [25].
Ti	Primary Al phase cell refinement effect from an addition of TiB ₂ [27].

Considering the Al-Si phase diagram (Figure 2.2), A365 is a hypoeutectic Al-Si alloy since the silicon content is lower than the eutectic composition ($\cong 12.6$ wt%). As a result, the microstructure would contain two phases: primary (α) Al and eutectic phases.

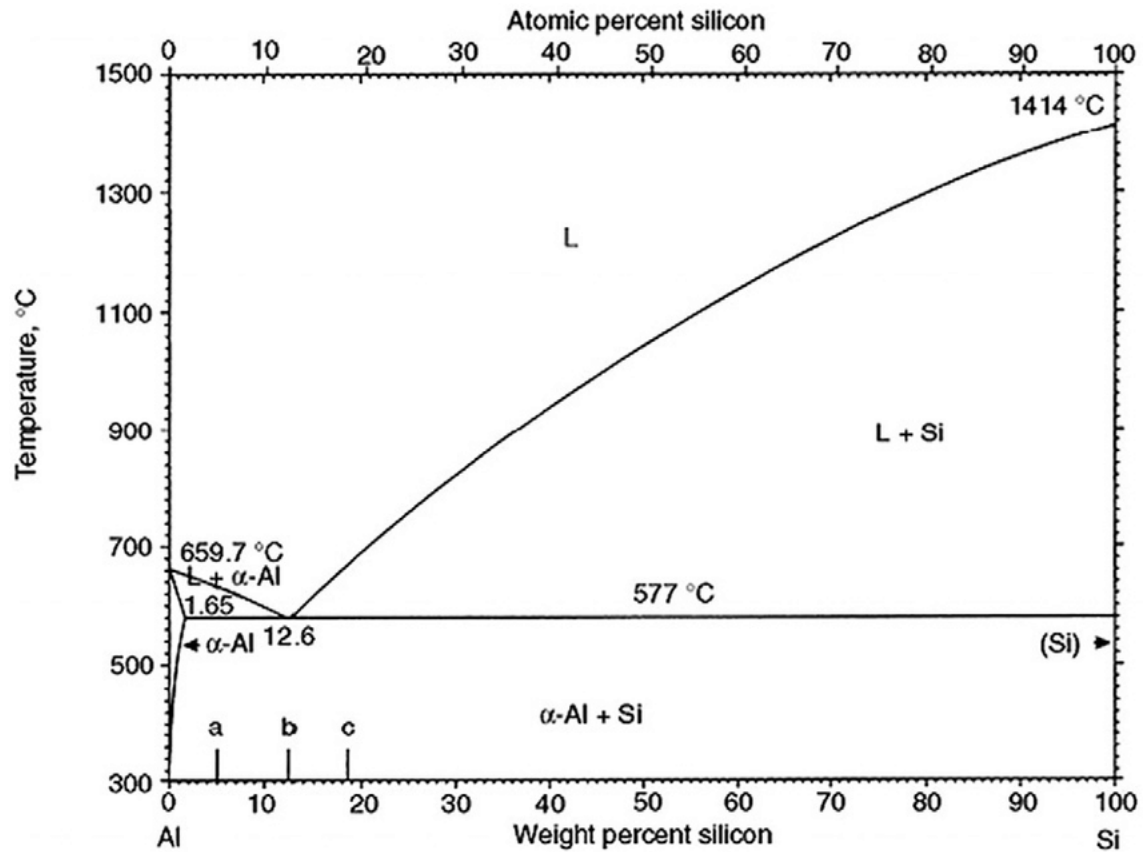


Figure 2.2: Al-Si phase diagram [28]

2.2 High Pressure Die Casting (HPDC)

HPDC is a casting method that involves injecting molten metal into cooled steel molds at high velocity and pressure. The applied pressure can range from ten to hundreds MPa, depending on the geometry of the casting and molten metal type [29]. HPDC also provides a high cooling rate; it varies from tens to thousands of degrees per second [30]. Due to its high efficiency, short production cycle, and flexibility of product geometry, HPDC is a practical casting method for manufacturing automotive components. HPDC also provides improved mechanical properties compared to permanent mold (PM) casting. Wan et al. [2] compared the microstructure and mechanical properties

of $AlMg_5Si_2Mn$ alloy produced by both HPDC and PM casting processes. It was demonstrated that HPDC provided a finer primary Al phase compared to PM casting, shown in Figure 2.3. Larger primary Al phase was observed in PM casting material in comparison to HPDC material due to the slower cooling rate. The volume fraction of Si eutectic phase observed in the HPDC material was increased by 7% in comparison to PM casting material. It was also observed that yield strength, ultimate tensile strength, and elongation were increased by 70%, 96%, and 192%, respectively.

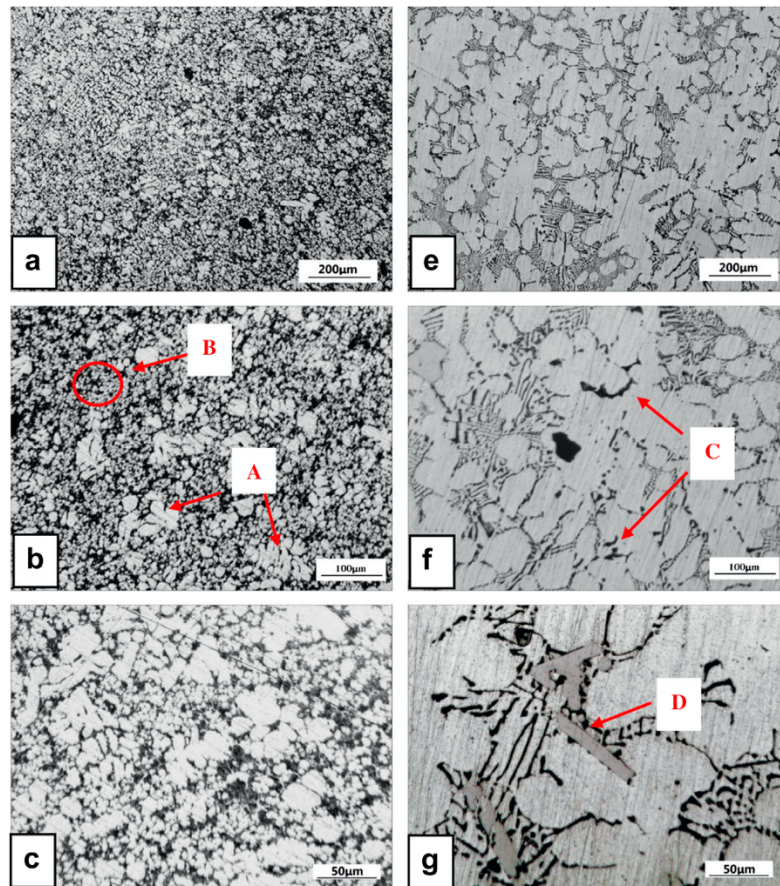


Figure 2.3: LOM image of the microstructure of HPDC (a-c) and PM (e-f) $AlMg_5Si_2Mn$,
A: Large primary Al phase, B: small primary Al phase, region C: $\alpha-Al_{15}(Mn, Fe)_3Si_2$,
D: $\beta-Al_5FeSi$ [2]

Despite the advantages, the HPDC process has several problems. One of the most detrimental problems is gas porosity formation. Gas porosity is formed due to a high concentration of air in the molten metal; air bubbles in the molten metal is entrapped during solidification due to applied high velocity and high pressure. The presence of gas porosity is undesirable, as it creates inconsistency in the microstructure, leading to degraded mechanical properties.

Incorporating a high vacuum system into the HPDC process (HVHPDC), was introduced to address the gas porosity formation issues. A high vacuum is applied to the injection chamber and die cavity in order to minimize the air bubble introduced during solidification [31], as shown in Figure 2.4.

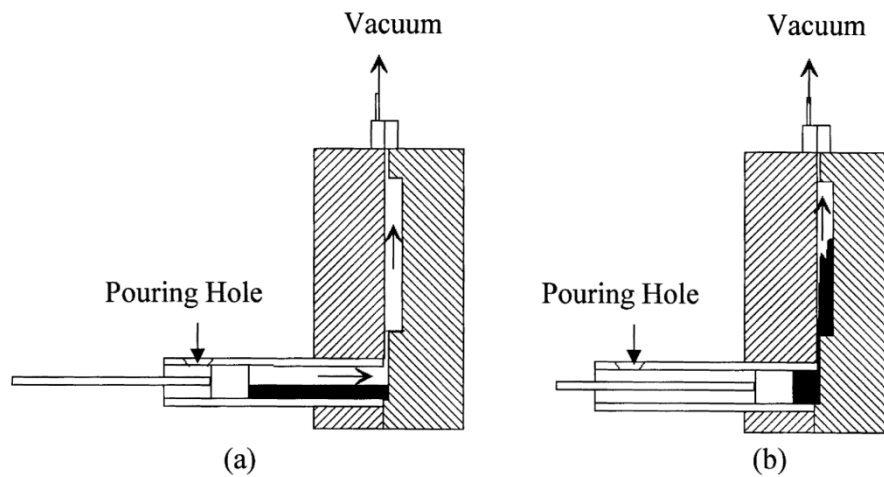


Figure 2.4: Schematic illustration of the HVHPDC process, (a): prior to molten metal injection (b): vacuum value activated while molten metal is injected into the cavity [31]

Several studies have investigated the benefits of HVHPDC versus conventional HPDC on mechanical properties of cast Al alloys. Niu et al. [31] investigated hypoeutectic Al-Si alloys and demonstrated that HVHPDC produced material, with increased density,

exhibited lower gas porosity formation. Wan et al. [32] investigated the mechanical properties of hypoeutectic AlMgSiMn alloys and argued that gas porosity (as observed in conventional HPDC material) was more responsible for the fatigue and crack propagation properties rather than yield strength and ultimate tensile strength. The improved mechanical properties of HVHPDC alloys were confirmed [32]. Dong et al. [33] investigated the repeatability of casting an AlSi8Mg alloy using HVHPDC in terms of casting quality. The improved quality and associated consistency were demonstrated by decreased variance in measured values of yield strength and ductility, relative to those acquired for conventional HPDC materials.

2.3 Heat Treatment and Microstructure of Al Alloy Castings

AA has established a temper designation system that indicates the various tempering procedures that are suitable for a given family of Al alloys to improve their mechanical properties. These treatments can be implemented mechanically, thermally, or both [20]. Table 2.4 lists the various temper designations and provides a description of each.

Table 2.4: Temper designation and description specified for Al alloys [19]

Temper Designation	Description
F	As-fabricated
O	Annealed
H1	Strain-harden
H2	Strain-harden and partially annealed
H3	Strain-harden and stabilized
T1	Cooled from an elevated temperature shaping process and naturally aged to a substantially stable condition
T2	Cooled from an elevated temperature shaping, cold worked, and naturally aged to a substantially stable condition
T3	Solution heat treated, cold worked, and naturally aged to a substantially stable condition
T4	Solution heat treated and naturally aged to a substantially stable condition
T5	Cooled from an elevated temperature shaping process and artificially aged
T6	Solution heat treated and artificially aged
T7	Solution heat treated and overaged or stabilized
T8	Solution heat treated, cold worked, and artificially aged
T9	Solution heat treated, artificially aged, and cold worked.
T10	Cooled from an elevated temperature shaping process, cold worked, and artificially aged.

The most used temper designations in heat-treatable Al alloy castings are T4, T6, and T7, each of which improves their mechanical properties relative to the as-cast (foundry) condition F. Generally, the T6 heat treatment produces the highest strength. The T4 heat treatment, which only requires a solution heat treatment followed by natural aging at room temperature after quenching, produces adequate mechanical properties with improved ductility, but significantly reduced strength, relative to the T6 heat treatment. The T7 heat treatment, involves a longer artificial aging time or a higher aging temperature than the T6 heat treatment. This heat treatment slightly improves strength, relative to the T4 heat treatment, without compromising the ductility. Figure 2.5

illustrates the effect of heat treatment process on their strength and ductility of A365.0 alloy.

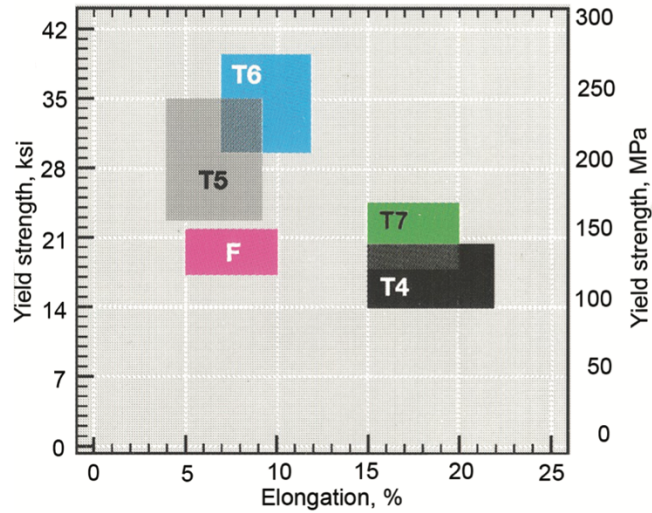


Figure 2.5: Variation of yield strength and elongation of Al alloy A365.0 with various heat treatments applied [21]

The microstructure of HVHPDC hypoeutectic Al-Si-Mg alloys can be modified by heat treatment, chemical composition, and HVHPDC process factors such as cooling rate, pressure level, and molten metal temperature. Figure 2.6 shows the microstructure of Al alloy A365, as well as the effect of heat treatment on the microstructure.

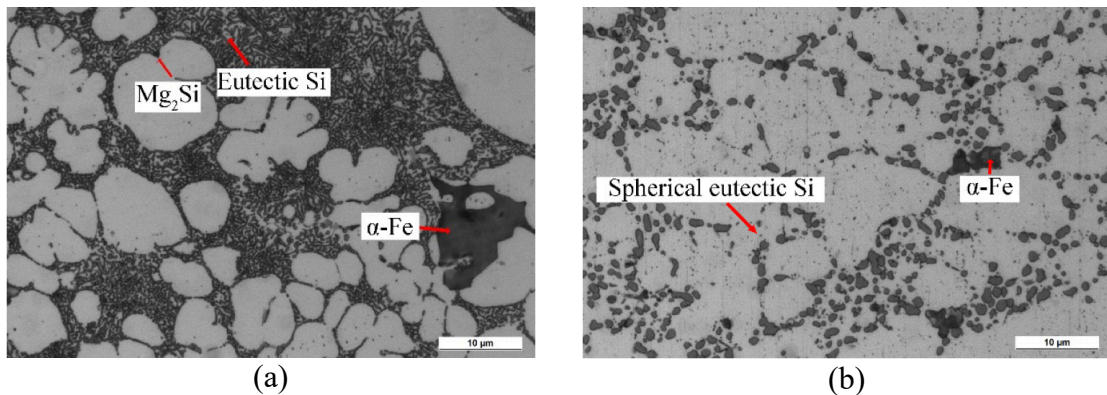


Figure 2.6: SEM microstructure images of A 365 alloy, (a): As-cast (b) T6 heat treatment [6]

After the T6 heat treatment, the morphology of Si eutectic phase was modified from plate-like to spherical. Mg_2Si was not observed on the T6 heat treated microstructure which was likely due to the solutionizing process; Mg_2Si was dissolved into primary Al phase [6]. α -Fe phase was observed on both of as-cast and post T6 heat treatment microstructure.

Heat treatment has significant impacts on microstructure. The main purposes of heat treatment on hypoeutectic Al-Si-Mg alloys are as follows:

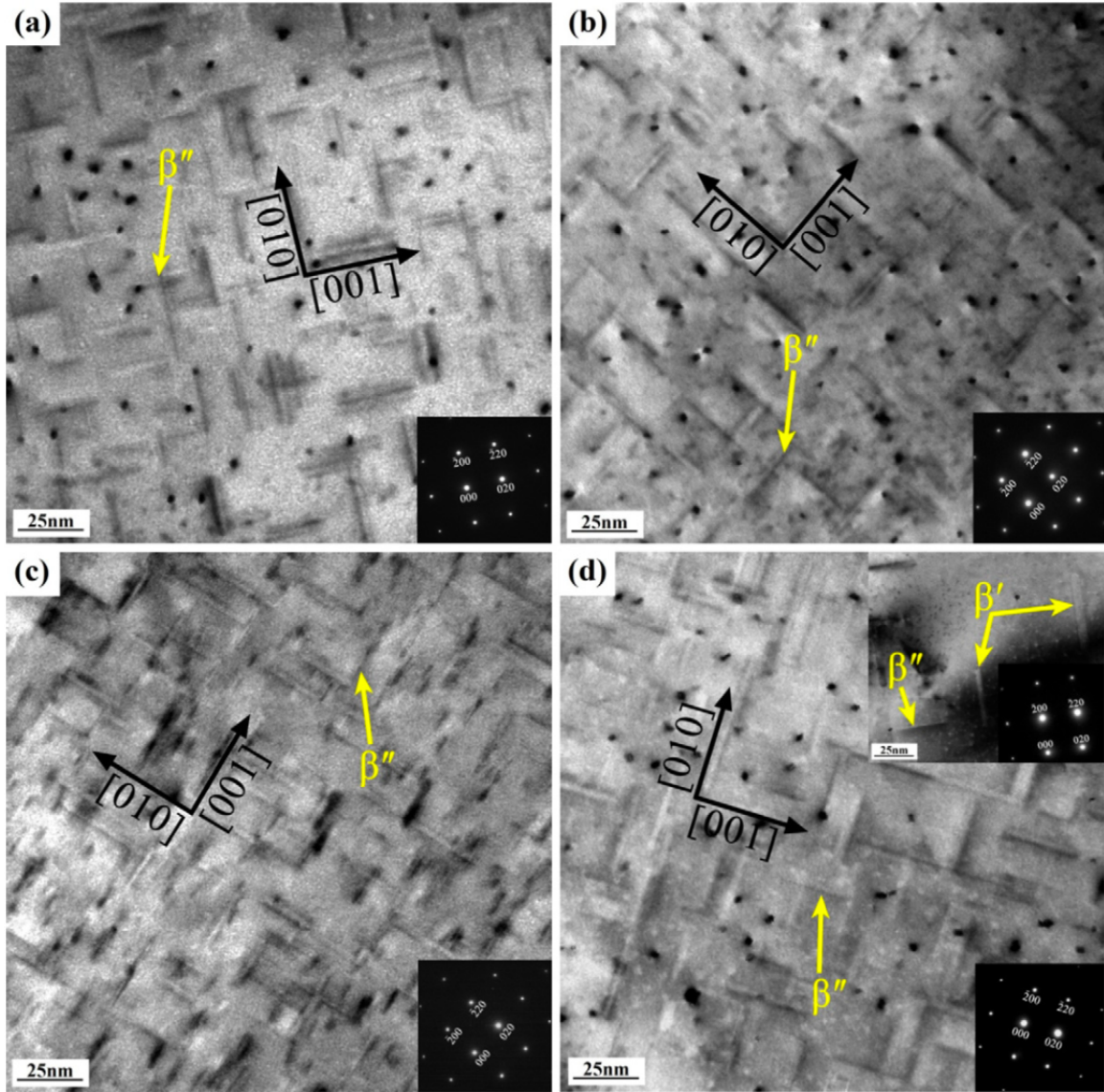
1. Dissolution of soluble phases for subsequent re-precipitation during controlled aging
2. Homogenization of alloying elements (reduce micro-segregation)
3. Spheroidization of Si eutectic phase for improving mechanical properties

Typical soluble phases observed in hypoeutectic Al-Si-Mg alloy castings include: β - Mg_2Si , π - $Al_8Mg_3FeSi_6$, θ - $AlCu_2$, α - $Al_{15}(Fe,Mn)_3Si_2$, and β - Al_5FeSi . The first step is a solution heat treatment. Temperature and time during this step should be selected to yield a homogenous solid solution structure. Fe-bearing phases are much difficult to dissolve during the heat treatment process compared to more soluble phases such as β - Mg_2Si and θ - Al_2Cu . The solid solution is necessary to subsequently precipitate the hardening phase (β - Mg_2Si) during controlled aging, then quenching is required to obtain supersaturated solid solution (SSSS) which contains a high concentration of solute atoms in the solvent [34]. The next step is aging, where a coherent (low interfacial energy) precipitate strengthening phase is formed. The microstructure can be heavily modified depending on

the aging temperature and time. The precipitation through the heat treatment is a very complex process and not fully understood, however, the initial formation of Guinier-Preston (GP) zone during the aging is well established [35] [36]. The sequence of precipitation hardening resulting from formation of the β -Mg₂Si phase is as follows:



GP zones are spherical fine-scale particles (1 – 2 nm size) formed during the first stage of aging process [37]. however, a complete understanding of GP zones such as the defined chemical composition and unit cell orientation is lacking [35]. β'' -Mg₂Si, β' -Mg₂Si, and β -Mg₂Si are coherent (low interfacial energy), semi-coherent (intermediate interfacial energy), and incoherent (high interfacial energy) Mg₂Si precipitates, respectively. β'' -Mg₂Si is a monoclinic, needle-shaped precipitates that is transformed to rod-shaped β' -Mg₂Si with aging time However, β' -Mg₂Si can precipitate without prior β'' -Mg₂Si precipitation Burger et al. [38] claimed that lath-shaped β' -Mg₂Si was formed at the GP zones independently with a prolonged aging heat treatment. Mechanical strength is improved when very fine heterogenous β' -Mg₂Si particles are precipitated [39]. β -Mg₂Si is a final formation of stable precipitates involving Mg₂Si particles. β -Mg₂Si is formed after the prolonged aging treatment, so-called over-aging. Figure 2.7 demonstrates the transmission electron microscopy (TEM) images of β' -Mg₂Si and β'' -Mg₂Si precipitates formed after the heat treatment. The artificial aging process of Figure 2.7-d sample was aimed to be over-aging; this was also confirmed with the formation of β' -Mg₂Si.



	(a)	(b)	(c)	(d)
Solutionizing Time (h)	6	8	10	8
Artificial aging time (h)	10	6	5	12

Figure 2.7: TEM images of β' - Mg_2Si and β'' - Mg_2Si precipitates with various solutionizing time (at 540 °C) and artificial aging time (at 175 °C) [40]

The presence of IMPs, has a critical impact on the microstructure, hence influences both mechanical and corrosion properties. Fe is observed in various IMPs in cast hypoeutectic Al-Si-Mg alloys. Fe is highly soluble in Al while it is molten, however, its solubility is significantly decreased Al when it solidifies, as shown in Figure 2.8.

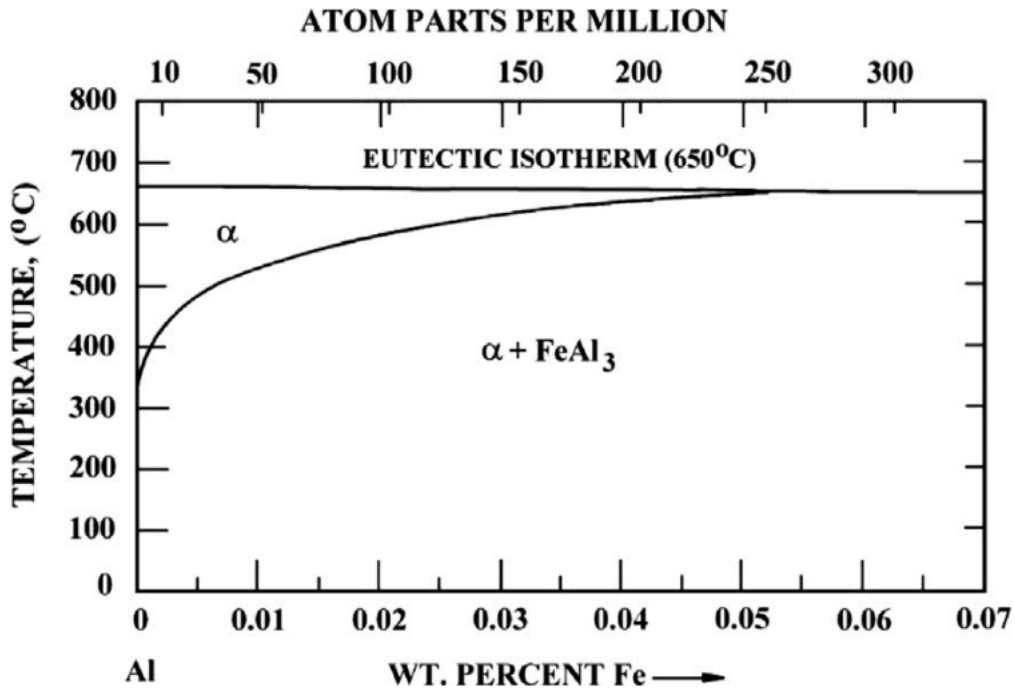


Figure 2.8: Phase diagram of Al-Fe system [41], showing the low eutectic composition of Fe in Al ($\cong 0.05$ wt%)

In cast hypoeutectic Al-Si-Mg alloys, the needle-shaped, brittle β -Al₅FeSi phase is detrimental to mechanical properties [42]. The α -Al₁₅(Fe,Mn)₃Si₂ phase, on the other hand, is round-shaped and less brittle than the β -Al₅FeSi phase, hence it is a more favourable IMP to maintain adequate mechanical properties [40] [42] [43]. Figure 2.9 demonstrates the morphology of β -Al₅FeSi and α -Al₁₅(Fe,Mn)₃Si₂. Table 2.5 shows the

precipitation sequence of Fe-bearing IMPs in hypoeutectic Al-Si alloy castings. The α - $\text{Al}_{15}(\text{Fe},\text{Mn})_3\text{Si}_2$ phase can solidify before and after primary Al dendrites; if solidified before, then is referred to sludge particles. Sludge particles are not desired since they can be incorporated within solidifying primary Al dendrites. This phase is typically observed when an extensive amount of Mn is available within the structure [13].

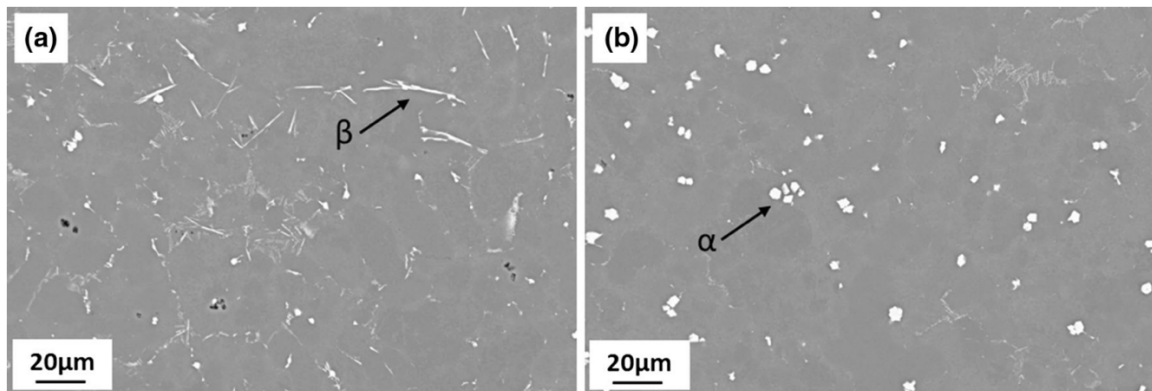


Figure 2.9: Microstructure images showing morphology of (a): β - Al_5FeSi , (b): α - $\text{Al}_{15}(\text{Fe},\text{Mn})_3\text{Si}_2$ [13]

Table 2.5: Precipitation sequence and solidification temperature of Fe-bearing IMPs [39]

Phase	Precipitation temperature ($^{\circ}\text{C}$)
α - $\text{Al}_{15}(\text{Mn}, \text{Fe})_3\text{Si}_2$ (sludge)	650
α -Al, α - $\text{Al}_{15}(\text{Mn}, \text{Fe})_3\text{Si}_2$	600
Al/Si eutectic, β - Al_5FeSi	550

An approach to control the morphology of Fe-bearing IMPs is an addition of Mn, which also reduce die soldering effect for Al alloy castings with low Fe content [44]. A summary of the morphology and associated effect of Fe-bearing IMPs, as observed in hypoeutectic Al-Si-Mg alloy castings on mechanical properties is shown in Table 2.6.

Table 2.6: Qualitative effect of Fe-bearing IMPs on mechanical properties of hypoeutectic Al-Si alloy castings [42]

IMP	Morphology	Effect on Mechanical Properties
β -Al ₅ FeSi	Monoclinic	Detrimental
α -Al ₈ Fe ₂ Si	Hexagonal	Less detrimental
α -Al ₁₅ (Fe,Mn) ₃ Si ₂	Cubic	Less detrimental

The so-called “skin effect” is a unique microstructure feature that can occur in the near-surface region HPDC/HVHPDC alloy castings. The effect is caused by a high cooling rate and premature solidification, resulting in a discrepancy in the microstructure between near-surface and core region [45]. One of the distinctive characteristics of the skin effect is the presence of a finer cell size of the primary Al phase in the near-surface region compared to the core. The skin region also contains a higher fraction of the Si eutectic phase, and coarse IMPs, which results in improved mechanical properties relative to the core region of the cast [46].

2.4 Localized Corrosion of Hypoeutectic Al-Si Alloy Castings

2.4.1 Cyclic potentiodynamic anodic polarization

Cyclic potentiodynamic anodic polarization is an electrochemical measurement that provides significant insight into the localized corrosion susceptibility in a given active/passive alloy in a solution containing an aggressive anion (typically Cl⁻ (aq)) . Figure 2.10 shows three typical conditions that could be observed during a cyclic potentiodynamic anodic polarization measurement.

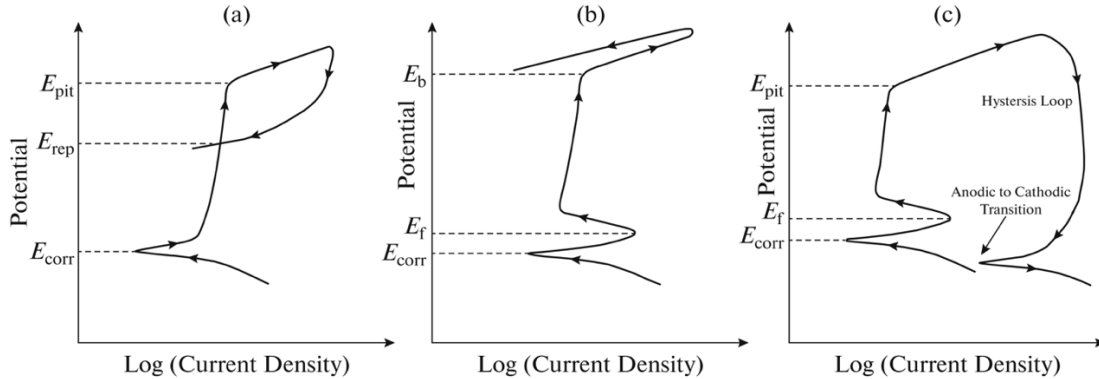


Figure 2.10: Illustration of cyclic polarization measurement behaviour, (a): with repassivation potential, (b) oxygen evolution, and (c) without repassivation potential [47]

Corrosion potential (E_{corr}) is the potential where cathodic current and anodic current are equal and there is no net current flow between cathodic and anodic regions [48]. Passive film is then formed after reaching E_{corr} , then enter the passive region where current density remains at the stable level while potential is increased. The role of passive film in localized corrosion initiation will be further discussed.

When the potential reaches to breakdown potential (E_b), localized corrosion is initiated. As shown in Figure 2.10 (a-c), current density is drastically increased due to localized breakdown of passive film. Above the E_b , stable localized corrosion is initiated. When localized corrosion is initiated, the corrosion sites can be either propagate or repassivate. When the reverse scan is applied, the potential can either reach repassivation potential (E_r), where protective passive layers are formed on the existed localized corrosion sites (Figure 2:10-a) or does not repassivate at all (Figure 2:10-c). Essentially, stable localized corrosion can initiate and grow above E_b , only existing localized corrosion can grow at

the potential between E_b and E_r . Below E_r , all localized corrosion sites are repassivated, as shown in Figure 2.11.

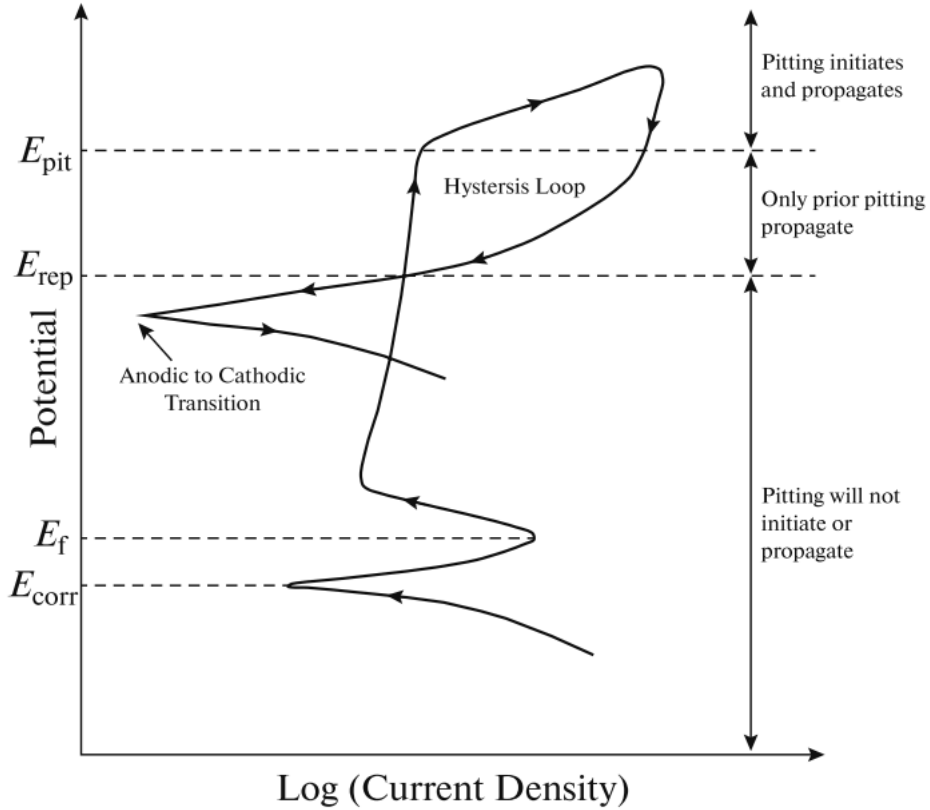


Figure 2.11: Cyclic polarization schematic with description of stable localized corrosion imitation and propagation [47]

Repassivation is a favourable when localized corrosion is induced; it provides a protective layer to stop stable growth. The difference between E_b and E_r (ΔV) can be interpreted as the tendency for repassivation; observing smaller ΔV values can indicate easier repassivation and, thus reduced localized corrosion susceptibility [47].

There are two types of localized corrosion: metastable and stable localized corrosion. Metastable stage refers to the localized corrosion formation at the potential where is

below E_b but above E_r . This can occur when the anions are aggressive enough to build the environment where anodic dissolution of passive metal is accelerated and enforced. The propensity of passive film breakdown increases with an increase in temperature and anion concentration, and a decrease in pH level of the surrounding environment [49] [50].

2.4.2 Passive film breakdown

When an exposed surface of an Al alloy reacts with oxygen molecules, a thin oxide film (Al_2O_3) so-called passive film forms and acts as protective layer against further oxidation [51]. The compositional stability of this passive film is extremely high on pure Al, however, is compromised when alloying elements are introduced [52]. The presence of eutectic phases and secondary phases at the exposed surface influences the consistency of passive film chemistry, which adversely affects passive film stability. Although passive film acts as protective layer against the further oxidation, it can break down locally to expose a small region of the metal surface, becoming boldly exposed to the electrolyte [53]. Under this scenario, the exposed metal dissolves as a local anode as it is coupled to the adjacent passive surface, which serves as the cathode [54]. The mechanism of localized corrosion is not fully understood, yet it is established that aggressive ions such Cl^- attack the passive film locally, which causes breakdown [55]. There are three main models that have been proposed to explain how Cl^- ions and passive film interact to promote passive film breakdown: penetration [56], absorption [57], and point defect mechanism [58]. Penetration mode relies on the Cl^- ions being aggressive enough to penetrate through the passive film to induce the breakdown. Absorption mode

is explained by Cl^- ions being absorbed through the passive film due to the presence of the oxygen vacancy within the passive film. Point defect mechanism is simply explained by the presence of pre-existing point defect within the passive film, which provides a high mobility path for Cl^- ions to damage the passive film. Passive film breakdown can be induced by one or a combination of those mechanisms.

2.4.3 Localized corrosion initiation

Fathi et al. [59] conducted a corrosion investigation of die-cast A360.1 alloy (AlSi9Mg0.5Mn0.35) and demonstrated that IMPs with Cu and Fe promoted localized corrosion initiation; it was explained with the enhanced anodic dissolution driven by the large corrosion potential differences between the IMPs and the primary Al phase.

Pech-Canul et al. [60] studied localized corrosion susceptibility of AlSi8Mg14 alloy under natural aerated NaCl solution and determined that localized corrosion was initiated around Fe-containing IMPs, shown in Figure 2.12.

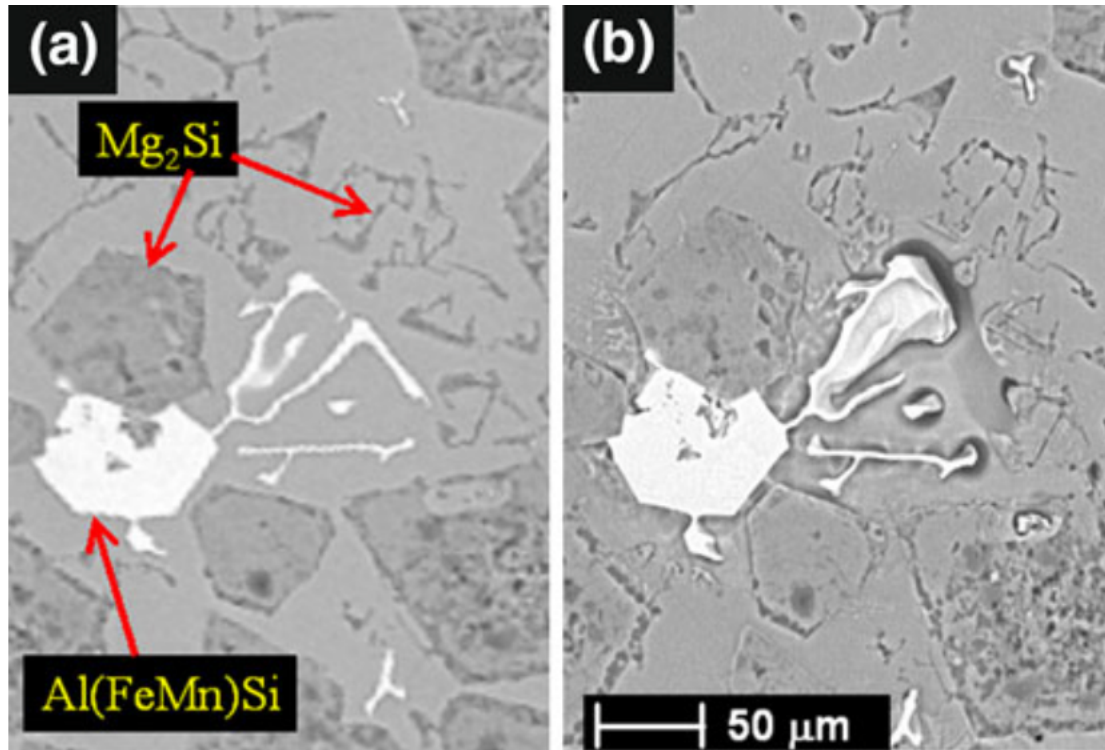


Figure 2.12: SEM images of AlSi8Mg14 alloy (a): before the NaCl solution immersion, (b): after the NaCl solution immersion [60]

Arrabal [8] et al. performed scanning Kelvin probe force microscopy (SKPFM) to acquire the Volta potential of several phases observed in rheocast A356 alloy (AlSi7Mg0.4) relative to the primary Al phase; the measurements are listed in Table 2.7. β -Al₅FeSi phase was most noble respect to the primary Al phase. π -Al₈Mg₃FeSi₆ exhibited less cathodic effect relative to the primary Al phase.

Table 2.7: Potential differences relative to primary Al phase, measured by SKPFM on A356 [8]

	β -Al ₅ FeSi (mV)	π -Al ₈ Mg ₃ FeSi ₆ (mV)	β -Mg ₂ Si (mV)
ΔV related to primary Al phase	+310 - +360	+120 - +140	-80 - -90

The effect of Mn on the electrochemical behaviour of Fe-containing IMPs was established by Nisancioglu [61]; the electrochemical behaviour of AlFe_3 and $\alpha\text{-Al}(\text{Mn}, \text{Fe})\text{Si}$ was compared with potentiodynamic polarization. It was discovered that Mn suppressed the effect of Fe by observing the anodic and cathodic current density as shown in Figure 2.13.

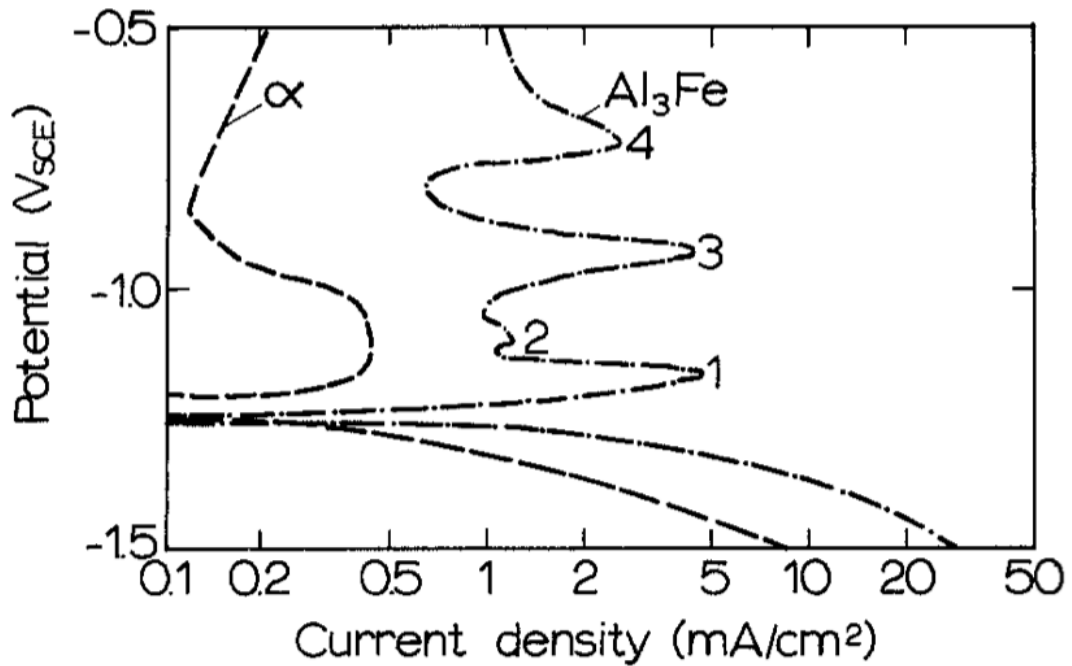


Figure 2.13: Potentiodynamic polarization curve of AlFe_3 and $\alpha\text{-Al}(\text{Mn}, \text{Fe})\text{Si}$ with 0.1 M $\text{Na}(\text{OH})$ solution, indicating the lower anodic and cathodic current density observed on $\alpha\text{-Al}(\text{Mn}, \text{Fe})\text{Si}$ [61]

Previous research work confirmed the localized corrosion susceptibility of hypoeutectic cast Al-Si-Mg alloys and suggested that Fe/Cu-bearing IMPs and effect of Mn content within the IMPs were critical features that determined localized corrosion initiation susceptibility.

2.4.4 Localized corrosion propagation

In hypoeutectic Al-Si alloy castings, when localized corrosion is initiated, the primary Al phase is selectively dissolved as an anode while the Si eutectic phase serves as the cathode to promote micro-galvanic corrosion [62]. Galvanic corrosion in general is triggered “when two metals or alloys having different compositions are electrically coupled while exposed to the electrolyte” [34]. Hence, it is extremely difficult to avoid when multiple phases exist within the microstructure. Ultimately, micro-galvanic corrosion within the microstructure drives localized corrosion. Hu et al. [2] explored the corrosion susceptibility of HPDC AlMg₅Si₂Mn and concluded the localized corrosion attack propagated along the eutectic regions. It was also criticized by Berlanga et al. [63]; the corrosion attack was selectively propagated at the eutectic regions, as shown in Figure 2.14-(a). Energy-dispersive x-ray spectroscopy (EDS) analysis detected the oxygen signal on the Si eutectic phase within the corrosion site, indicating the preferential corrosion phenomena on the eutectic phase [63], as shown in Figure 2.14-(b) and Table 2.8.

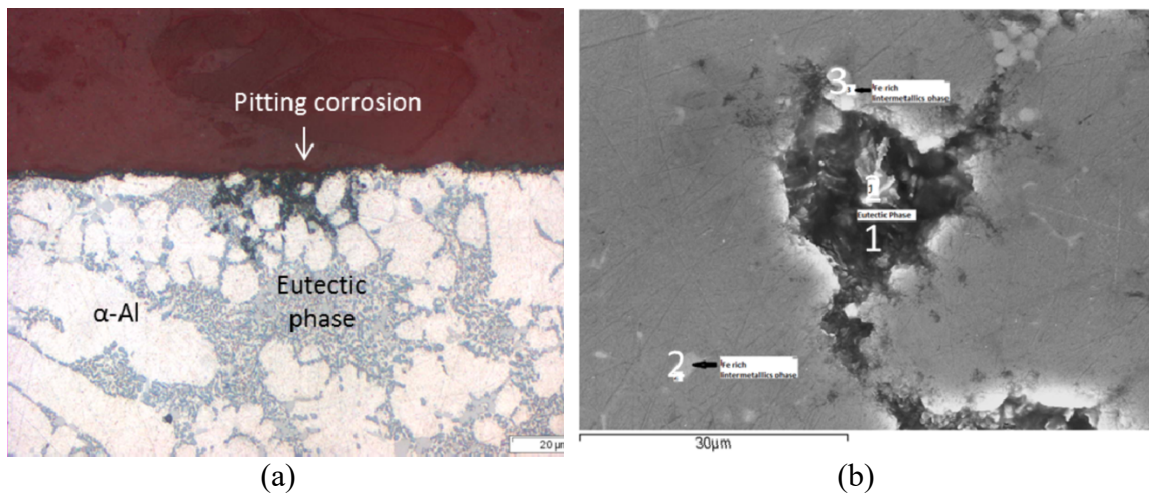


Figure 2.14: (a) LOM image of cross section of post corrosion test (b) SEM image of corrosion site (after potentiodynamic anodic polarization with 0.5 M NaCl solution) [63]

Table 2.8: EDS point analysis on eutectic phase and IMPs [63]

Spot Number	Al	Si	Mn	Fe	O
1	47.4	45.6	-	-	6.9
2	74.3	13.4	8.7	3.6	-
3	57.4	26.9	10.9	4.7	-

Although localized corrosion propagation occurs along the eutectic phases, it is crucial to understand the electrochemical behaviour of primary Al phase and eutectic phase. By observing the phase diagram of Al-Si system (Figure 2.2), the sequence of solidification can be expected as follows: α -Al phase, Al-rich eutectic phase, and Si-rich eutectic phase. Si-rich eutectic contains the highest Si content while it is practical to anticipate that Al-rich eutectic phase contains less Si content in comparison to Si eutectic phase. The specific electrochemical characteristics of those eutectic phases may not be fully determined, however, the major difference between the two phases is the Si content within their structure. Birbilis et al. [64] reported the corrosion potentials of pure Al and pure Si with 0.1 M NaCl electrolyte; the reported values were $-0.441 V_{SCE}$ and $-0.823 V_{SCE}$ for pure Si and pure Al, respectively. Considering those values, Al-rich eutectic phase (low Si content) is expected to be anode where Si-rich eutectic phase (high Si content) serves as cathode.

2.5 Secondary Hypoeutectic Al-Si-Mg Alloy Castings

Arguably, the major challenges with incorporating EOL materials to produce secondary alloy components via the HVHPDC process is impurity control. Impurity elements such as Fe, Cu, and Zn can be unintentionally introduced [65], which strongly

affect the microstructure of secondary Al alloys. Impurity elements and IMPs control is crucial in the fabrication of secondary Al alloys to secure their properties.

2.5.1 Mechanical properties of cast secondary Al-Si-Mg alloy

It is well understood that β -Al₅FeSi is detrimental to mechanical properties due to its low ductility. A fraction of β -Al₅FeSi within the cast is expected to increase as Fe content in the cast Al-Si-Mg alloy is increased. Mn is typically added to modify the morphology of Fe-bearing IMPs, leading to an increase in ductility of IMPs. Wieszala et al. [66] investigated the effect of Mn addition on IMPs of cast secondary AlSi10Mg alloy and claimed that an addition of 0.6 wt% Mn effectively modified the IMPs morphology from β -Al₅FeSi to α -Al₁₅(Fe,Mn)₃Si₂ while containing 0.5 wt% Fe in AlSi10Mg alloy. It was also reported that yield strength and elongation was increased from 143 MPa to 272 MPa and 5.5 % to 7.9 %, respectively.

Bosch et al. [13] also investigated the effect of Mn addition on ductility of HPDC secondary Al-Si-Mg alloys and constructed the calculated phase fraction of α -Al₁₅(Fe,Mn)₃Si₂ and β -Al₅FeSi with respect to Mn content as shown in Figure 2.15. The graph illustrates that 0.5 % Mn (Mn/Fe \cong 1) is sufficient to mitigate the formation of β -Al₅FeSi. In contrast, an excess amount of Mn addition causes the sludge formation, hence, it was concluded that the appropriate balance between Mn and Fe leads to improvement on the mechanical properties of secondary alloys.

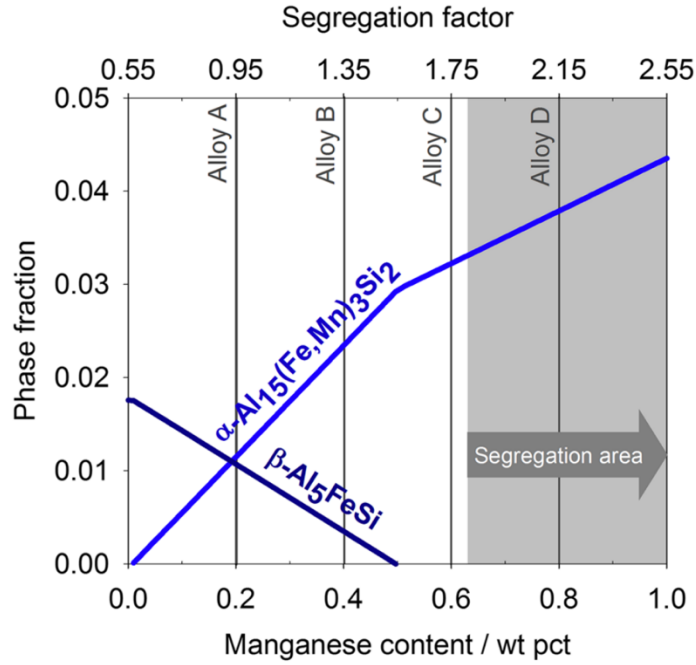


Figure 2.15: Phase fraction of α -Al₁₅(Fe,Mn)₃Si₂ and β -Al₅FeSi as a function of Mn content. The model is AlSi10.5Mg0.4Fe0.55-Mn at equilibrium condition. Segregation factor = Fe + 2Mn + 3Cr [13]

Lenka et al. [1] studied the microstructure of Mn-added secondary AlSi9Cu3 alloy and also determined that Mn addition resulted in a formation of desired α -Al₁₅(Fe,Mn) within their microstructure.

There were several trials to fabricate secondary A365 alloys to investigate their mechanical properties. The chemical compositions of those secondary A365 alloys are tabulated in Table 2.9.

Table 2.9: Chemical composition of developed secondary A 365 alloys (Fe Enrichment Factor = Fe content of secondary / Fe content of primary alloy (=0.2))

	Si	Mg	Fe	Mn	Cu	Zn	Sr	Fe Enrichment Factor
A365	9.5	0.27	0.15	0.45			0.01	1
	–	–	–	–	< 0.03	< 0.03	–	
	11.5	0.33	0.2	0.55			0.016	
Alloy 1 [15]	8.6	0.32	0.44	0.22	0.32	0.15	0.008	2.2
Alloy 2 [67]	10.1	0.37	0.62	0.42	0.04	0.03	0.01	3.1

Cinkilic et al. [15] developed a new secondary Al-Si-Mg alloy for structural die casting application. Microstructure and mechanical properties were compared to commercial structural cast Al-Si-Mg alloys.

The microstructure of their as-cast secondary alloy contained primary Al phase, α -Al₁₅(Fe,Mn)₃Si₂ / α -Al₈Fe₂Si, as well as π -Al₈FeMg₃Si₂, which had a needle-shape morphology. The θ -Al₂Cu phase was also observed within their microstructure, which was predictable considering its Cu content in their alloy. It was stated that Fe-to-Mn ratio of between 1.6 to 3 with rapid cooling condition can suppress β -Al₅FeSi phase formation based on their result. The mechanical properties of all investigated alloy are tabulated in Table 2.10.

Table 2.10: Mechanical properties of secondary alloy investigated by Cinkilic et al. [15]

Heat Treatment	Yield Strength (MPa)	UTS (MPa)	Elongation (%)
As-cast	154 ± 8	274 ± 10	5.8 ± 0.9
T5	194 ± 11	290 ± 16	3.7 ± 0.4
T6	173 ± 9	275 ± 5	7.8 ± 1.2

The mechanical properties of their new alloy were comparable to some commercial A365 alloys for as-cast condition [68], however, were slightly lower for heat-treated conditions. The elongation of their new alloy was heavily compromised; it was likely caused by a larger fraction of Fe-bearing IMPs due to its elevated Fe content. Nevertheless, it was concluded that the mechanical properties of their novel secondary alloy with T6 heat treatment were close to those of primary alloy.

Niklas et al. [67] also compared the mechanical properties of their secondary alloy with commercial primary A365 alloy and determined that they were comparable after the addition of sufficient amount of Mn. Addition of Mn content of approximately 2/3 of Fe content was crucial to mitigate the formation of β -Al₅FeSi within the microstructure, leading to the improved mechanical properties of secondary alloys [69].

Current research and development of cast secondary Al-Si-Mg alloys has established that the addition of Mn played a crucial role to affect the morphology of IMPs and mechanical properties. Although the optimized Fe-to-Mn ratio for cast Al-Si-Mg alloys was not entirely established, secondary alloys have shown mechanical properties that were comparable to primary alloy. However, it should be noted that Fe content in cast secondary Al-Si-Mg alloy of current research work was relatively high (> 0.4 wt%) compared to the commercial A365 alloys (< 0.2 wt%) [68].

2.5.2 Corrosion behaviour of cast secondary Al-Si-Mg alloys

Kucharikova et al. [17] determined that the corrosion susceptibility of secondary AlSi7Mg0.3 alloy was enhanced compared to primary alloy due to the elevated Fe

content observed on the secondary alloys. A higher Fe content in the secondary alloy led to a higher fraction of Fe-containing IMPs within the microstructure, resulting in an increase in the micro-galvanic corrosion induced between the primary Al phase and Fe-bearing IMPs [70]. Berlanga et al. [63] investigated the corrosion susceptibility of secondary A365 alloy as a function of wall thickness. The chemical composition of the investigated secondary A365 alloy is shown in Table 2.11.

Table 2.11: Chemical composition of investigated secondary A 365 alloy (Fe Enrichment Factor = Fe content of secondary / Fe content of primary alloy (=0.2))

	Si	Mg	Fe	Mn	Cu	Zn	Sr	Fe Enrichment Factor
A365	9.5	0.27	0.15	0.45			0.01	1
	–	–	–	–	< 0.03	< 0.03	–	
	11.5	0.33	0.2	0.55			0.016	
Alloy 1 [63]	10.1	0.37	0.62	0.42	0.05	0.03	0.01	3.1

It was concluded that the corrosion of the primary and secondary alloy was comparable with each other, in terms of mode and extent. Cecchel [18] investigated secondary A359 alloys which were subjected to electrochemical polarization to evaluate the localized corrosion mechanism. Figure 2.16 demonstrates that localized corrosion propagation was observed along the eutectic phase, both on skin and core regions.

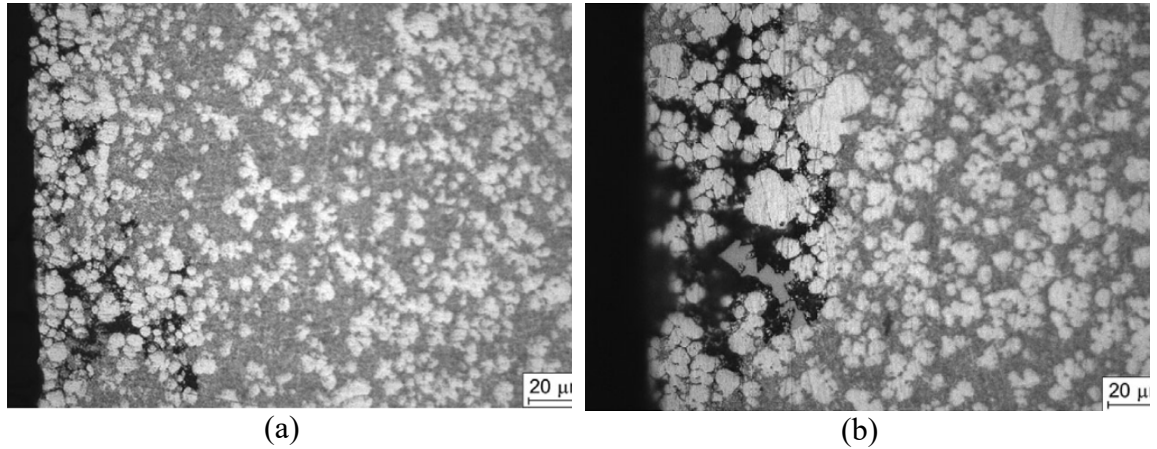


Figure 2.16: LOM images of cross section of post corrosion test, (a): skin region (b): core region of secondary A359 alloys (cyclic polarization with 0.05M NaCl solution) [18]

It was evident that despite the research conducted on the mechanical properties of cast secondary Al-Si-Mg alloys, corrosion susceptibility has not been thoroughly investigated. It was yet reasonable to suppose that corrosion susceptibility of secondary Al alloy was also influenced by morphology, chemistry, and distribution of IMPs as well. Previous investigations have confirmed that secondary Al alloys are more prone to corrosion; all of which attribute this increased susceptibility to an elevated Fe content. In other words, secondary alloys with controlled Fe content should have a similar corrosion susceptibility to the primary alloy.

Chapter 3: Research Objective

The corrosion propagation mechanism of primary and secondary alloys is expected to be similar, however, it is anticipated that either localized corrosion initiation mechanism of secondary A365-T7 alloy differs from the primary alloy, or the localized corrosion propagation kinetics may be enhanced in secondary A365-T7 alloy. Moreover, it is yet still not well explained how EOL content in the secondary A365-T7 alloys, with the same Fe content as the primary alloy, affects localized corrosion susceptibility. Moreover, localized corrosion indications on the post salt fog experiment samples can be distributed as localized corrosion is a complex three-dimensional phenomenon. Relying solely on the measured pitting depth on one two-dimensional (planar) cross section may not provide a true representation of localized corrosion susceptibility.

The objectives of this research are as following:

1. To characterize the microstructure feature of skin and core region of each EOL alloy to observe the differences in primary Al cell size, Si eutectic distribution, IMP morphology, chemistry, and distribution.
2. To characterize the localized corrosion susceptibility using various electrochemical polarization techniques and corrosion visualization experiment. Characteristic potentials regarding localized corrosion susceptibility were experimentally obtained by cyclic potentiodynamic polarization. Potentiostatic polarization was done to reveal the localized corrosion mode. Galvanostatic anodic polarization was conducted to observe the potential responses associated with initiation and propagation differences between each EOL alloy. Metastable

current density transients were obtained to evaluate the metastable localized corrosion initiation susceptibility. Finally, corrosion visualization through agar gel experiment was conducted to reveal the initiation differences between each EOL alloy.

3. To establish the metallurgical critical factor(s) controlling initiation and/or propagation by performing post-exposure examination of corroded samples with LOM, SEM-EDS, as well as passive film investigation through XPS analysis.

Chapter 4: Experimental Procedure

4.1 Materials

Thin-walled plate samples (3.0 mm thick) of secondary A365 alloys with different EOL contents (0%, 40%, 75%, and 90%), as produced using a HVHPDC process, were provided in the T7 temper by Nematik. Note that the EOL 0 alloy denoted the primary alloy. The chemical composition of each EOL alloy was determined by inductively coupled plasma – mass spectrometry (ICP-MS). Samples of each were sent to Cambridge Materials Testing Laboratory (Cambridge, ON) for this purpose. The chemical compositions of EOL alloys are shown in Table 4.1.

Table 4.1: Chemical composition of EOL alloys, obtained by ICP-MS analysis (wt%)

	Si	Mn	Mg	Fe	Cu	Ti	Zn	Fe Enrichment Factor
EOL 0	11.03	0.56	0.30	0.18	0.01	0.07	0.00	1
EOL 40	10.59	0.49	0.31	0.17	0.07	0.03	0.02	0.94
EOL 75	10.57	0.52	0.33	0.18	0.07	0.03	0.02	1
EOL 90	10.27	0.52	0.34	0.18	0.07	0.04	0.01	1

Fe content of all secondary alloys was found to be at the similar level with primary alloy. Cu and Zn contents of all secondary alloys, however, were slightly elevated in comparison to primary alloy. Additionally, lower Ti content was detected on all secondary alloys.

4.2 Microstructure Characterization

Both planar (L-T plane) and through-thickness (TT) views of each EOL alloy were isolated and cold-mounted in epoxy. The example of direction orientation of the plate sample is shown in Figure 4.1.

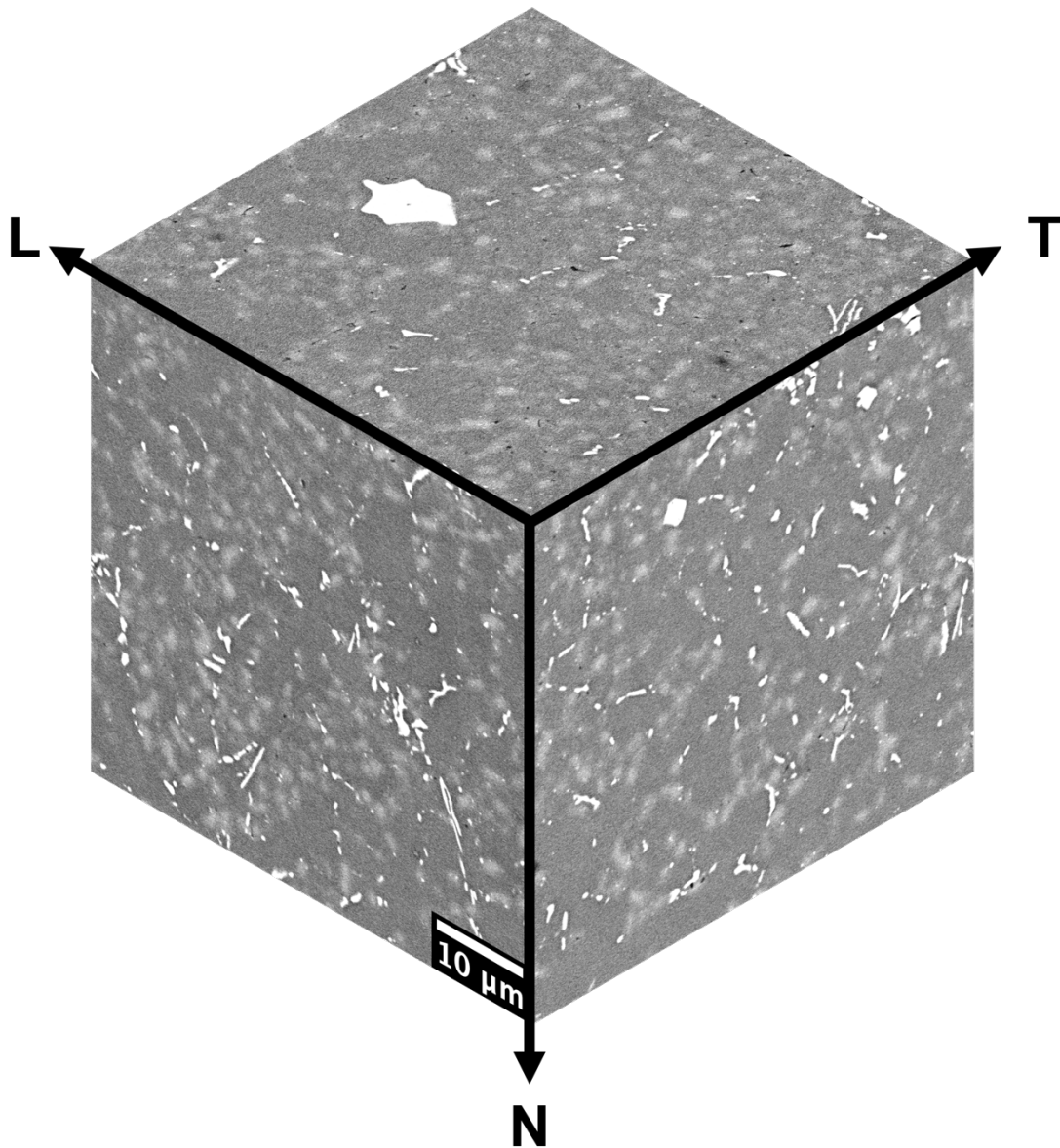


Figure 4.1: SEM-backscatter electron (BSE) image of EOL 0, describing the direction orientation of the cast

The working surfaces were mechanically-abraded to a 320 grit surface finish using SiC abrasive paper and water as a lubricant, then fine polished with 9 μm and 3 μm polycrystalline diamond suspension, in series, using an ethanol-based lubricant (blue lubricant). Final polishing to a mirror surface finish was achieved using a water-free silica colloidal suspension (OPS). Ultrasonic cleaning with acetone was applied between each step of grinding and polishing.

For LOM examination, polished surfaces were etched with Keller's etchant (190 mL of distilled water, 5 mL of HNO_3 (aq), 3 mL of HCl (aq), and 2 mL of HF (aq)) to reveal the microstructure. The etchant was applied for 8 to 16 s. Images of the etched surfaces were acquired using a Keyence VHX 5000 digital microscope. Figure 4.2 illustrates the imaging process conducted with imageJ for primary Al cell size measurement.

Microstructure images were converted to 8-bit images (Figure 4.2-(a)) then processed to reveal the primary Al phase (Figure 4.2-(b)). Horizontal lines were drawn on the processed images, then distance between two interceptions was interpreted as primary Al cell size (Figure 4.2-(c)). A total of 100 measurements were collected for both skin and core region of each EOL alloy to ensure the statistical measurement.

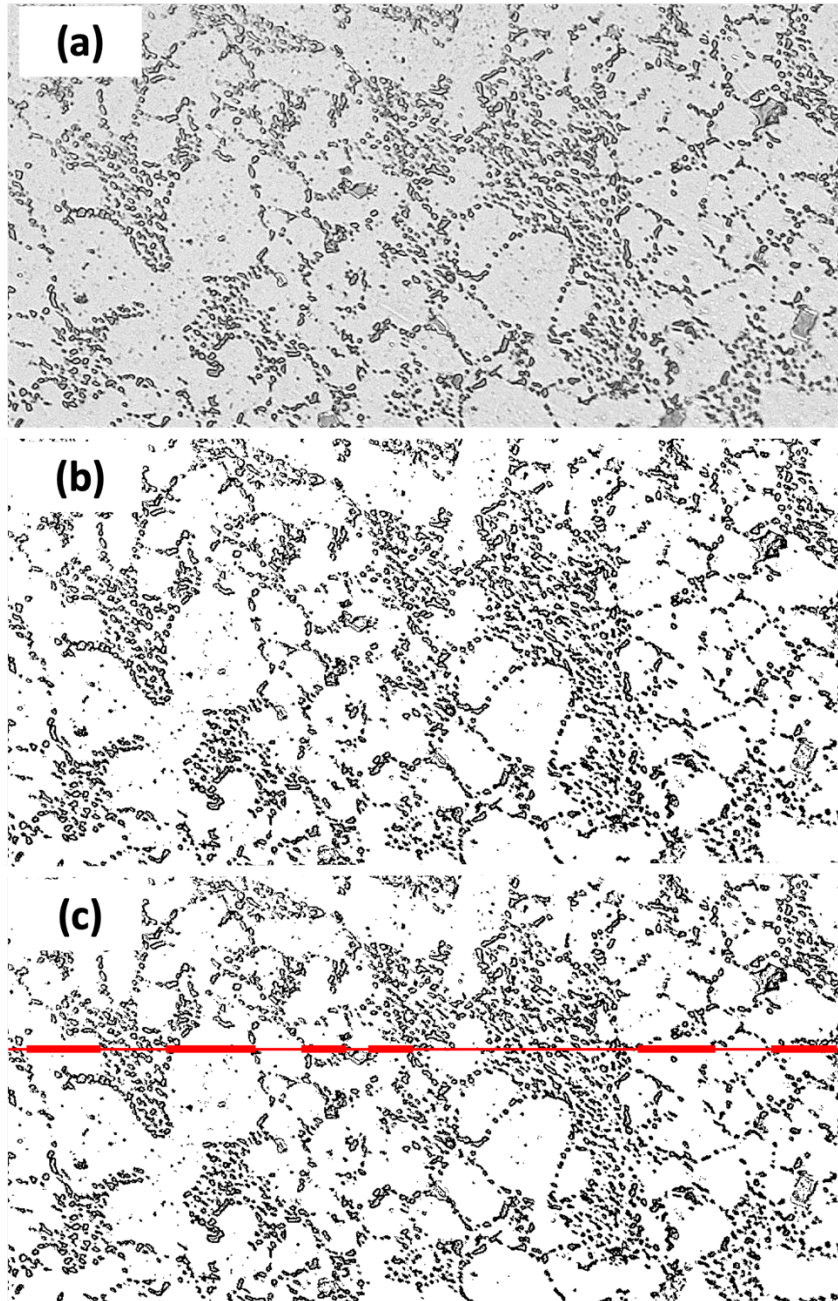


Figure 4.2: Imaging process of primary Al cell size measurement, (a): 8-bit image (b): processed image revealing Al dendrite (c): linear interception for cell size measurement, thick red line indicating the primary Al cell size

For SEM examination, polished surfaces were coated with C and Ni paste was applied to provide the conductive path, ensuring the analysis quality. Both secondary electron (SE) and BSE images were acquired at various magnifications using JOEL 6610 LV instrument. The source energy, working distance, and spot size were set at 10 keV, 10 mm, and between 45 to 60 nm depending on the resolution and calibration, respectively. EDS was also used to obtain elemental (composition) information. All EDS data such as spot analysis and map acquisition were obtained using an Oxford Instruments EDS system (incorporated into the JEOL 6610LV instrument) and associated Aztec software. Microstructure images were analyzed using the ImageJ software to determine specific distributions such as the Si eutectic network, coarse IMPs, and primary Al cell size.

4.3 Corrosion Experiments

4.3.1 Electrochemical Polarization

Small square samples (1 cm x 1 cm, L-T plane) were cut from the as-received plate material to fabricate the working electrodes. A length of insulated Cu wire was attached to one of the faces of each sample to make the necessary electrical connection. The sample was then cold-mounted in epoxy with the other face serving as the working surface (exposing the L-T plane). After curing, the working surface was prepared by mechanically-abrading to a 600 grit surface finish using SiC abrasive paper and water as a lubricant. Samples were then cleaned with degreasing cleaner and rinsed with ethanol. For the investigation of the core region, mounted samples were mechanically-abraded with a 240 grit SiC abrasive paper until the thickness of mounted sample was reduced by

1mm. The working surface was then prepared by mechanically-abrading to a 600 grit fishing using SiC abrasive paper and as water as a lubricant.

An electrolyte solution consisting of 0.5 M NaCl (aq) was used for all electrochemical polarization measurement. It was made using reagent grade NaCl crystals and deionized water. All polarization measurements were performed using a computer-controlled Gamry Potentiostat Reference 600/600+ potentiostat/galvanostat coupled with a conventional three electrode electrochemical cell (1000 mL capacity). A graphite rod was used as the counter electrode and a saturated calomel electrode was used as the reference electrode. All electrochemical polarization measurements were conducted at least in triplicate to ensure reproducibility. The electrolyte solution was deaerated by sparging with high purity nitrogen gas for the duration of each measurement, beginning 0.5 h prior to the start of a given measurement.

Cyclic potentiodynamic polarization curves were acquired using a scan rate of 0.167 mV/s. The scan was initiated after conditioning the working surface at the open circuit potential (OCP) for a period of 1.0 h. The starting potential for the forward scan was set at 0.1 V below the measured OCP. The apex current density, where the reverse was initiated, was set at +0.1 mA/cm².

Potentiostatic polarization measurements were conducted on the skin region for 4.0 h with an applied potential of 50 mV above the E_b obtained by cyclic potentiodynamic polarization. After polarization measurement, a working surface was cut in through cross-section, cold-mounted, and ground and polished to a mirror finish using the procedure described above (Section 4.2).

Galvanostatic anodic polarization measurements were conducted on the skin region using an applied current density of $+1 \text{ mA/cm}^2$ for 5.0 h. The potential transient was recorded at a collection frequency of 1.0 Hz. Galvanostatic anodic polarization was initiated after conditioning the working surface at OCP for a period of 1.0 h. After polarization, the working surface was cut in cross-section, cold-mounted in epoxy, and ground and polished to a mirror finish using the procedure described above (Section 4.2). The polished surfaces were imaged using the Keyence VHX 5000 digital microscope to document the corrosion mode and extent.

EOL 0 and EOL 40 were further investigated for metastable pitting susceptibility (skin surface only). Working surfaces were potentiostatically polarized for 3.0 h at the applied potential of 20 mV below the E_b obtained from cyclic potentiodynamic polarization measurements. Potentiostatic polarization was initiated after conditioning the working surface at OCP for a period of 1.0 h. The responsive current density was recorded at a frequency of 1.0 Hz.

4.3.2 Corrosion Visualization

A solid agar gel-based electrolyte, consisting of 2% agar powder, 5% universal pH indicator and 3.0 M NaCl (aq) was prepared using reagent grade chemicals and deionized water. The water was heated to 90°C and agar powder was slowly poured in. After the agar powder was completely dissolved, NaCl crystals and universal pH indicator were then added to the mix. The working surface (L-T plane) was cleaned with acetone and ethanol prior to applying the solid agar electrolyte. The thickness of agar gel was

controlled at 1 cm, and the working surface was 4 cm x 4 cm; the non-conductive tape was applied to working surface to ensure the geometry of exposed surface. The agar solution was poured into a cast in place and cooled until solidified. The solidified agar gel was cut into 4 cm x 4 cm, then applied to the working surface. Digital images of agar electrolyte-covered working surface were taken every hour for 4 h. This corrosion visualization test was conducted to observe the anodic and cathodic regions as revealed by colour change associated with the universal pH indicator. The number of red regions (acidic - anodic sites) identified localized corrosion initiation sites.

4.3 X-Ray Photoelectron Spectroscopy (XPS)

XPS analysis was conducted to investigate the structure and composition of the passive film formed during potentiostatic anodic polarization. Small disc samples (1.5 cm diameter) were prepared from the as-received EOL 0 and EOL 40 plate material. Working electrodes (L-T plane) were prepared in the same way as described above (Section 4.2). The working surface was conditioned at the OCP 1.0 h before being potentiostatically polarized at $-0.9 V_{SCE}$ for 1.0 h to form the passive film. After polarization, the working surface was cleaned with ethanol. XPS analysis was conducted using a PHI Quantera II Scanning XPS Microprobe. Micro-focused Scanning x-ray source was utilized with a condition of 12.5 W (X-ray power) and 15 kV (X-ray energy). Step size of 0.8 eV was used for survey scanning, and 0.1 eV for all elemental analysis. Cleaning (sputtering) was applied to remove all adventitious C signals on the spectrums. Survey scanning was performed on three different spots to ensure the consistency of the analysis. Take-off

angle was set at 45°. All the spectra, curve fittings, and the positions of spectrum peaks were generated and obtained within the analysis software.

Chapter 5: Results

5.1 Starting Microstructure Characterization

The entire cross-section images of each EOL alloy are shown in Figure 5.1. The off-white-coloured phase is primary Al phase, and the dark grey colour phase is Si eutectic phase. Overall, the casting quality was not affected by the EOL content; major casting defects such as hot tearing cracks or porosity were not observed in any of the three secondary EOL alloys (EOL 40, EOL 75, and EOL 90). The major feature demarking the skin from the core was the size of the primary Al phase, which was smaller in the skin regions, as observed in all four EOL alloys.



Figure 5.1: Microstructure images of each EOL alloy obtained by LOM, cross section view. Red dotted lines demark the interface between the skin (located on either side) and the core

Figure 5.2 shows a high magnification LOM image of the skin and core observed in each of the four EOL alloys. Spheroidization of Si eutectic phase was observed in both the skin and core of each EOL alloy, indicating that the EOL content did not affect the spheroidization that occurred during the T7 heat treatment applied after casting. The primary Al phase cell size of the skin and core of each EOL alloy is listed in Table 5.1. The error bars represent the 95% confidence interval. The cell size was smaller in the skin, relative to the core, in each case. The EOL content did not affect cell size in the skin any consistent way. However, it did affect the cell size of the core, as the cell size decreased with an increase in the EOL content.

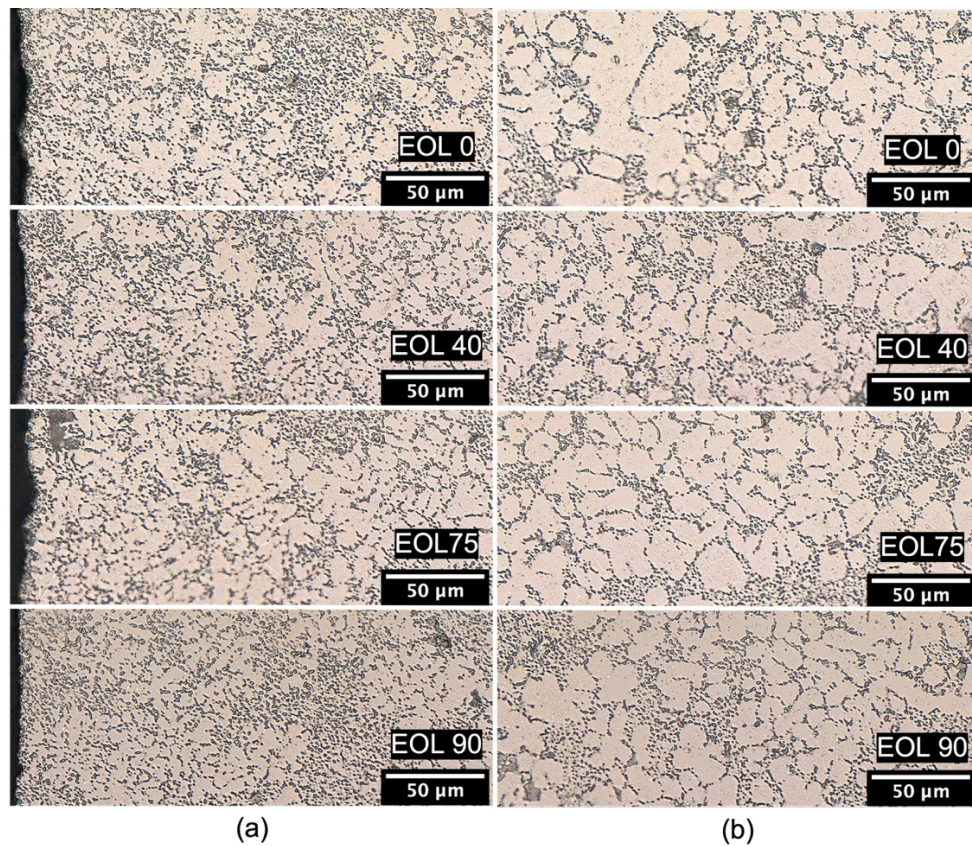


Figure 5.2: Cross sectional microstructure images of each EOL alloy: (a) skin and (b) core

Table 5.1: Primary Al phase cell size in the four EOL alloys

Alloy	Skin (μm)	Core (μm)
EOL 0	7.5 ± 0.7	21.1 ± 1.9
EOL 40	12.9 ± 0.9	17.0 ± 1.5
EOL 75	10.5 ± 0.8	16.9 ± 1.7
EOL 90	9.5 ± 0.7	13.3 ± 1.0

Figure 5.3 and Figure 5.4 shows a BSE image of the skin and core, respectively, observed in each of the four EOL alloys. The dark-grey regions, light-grey rounded regions, and white-bright particles in the BSE images represent the primary Al phase, Si eutectic phase, and Fe-bearing IMPs, respectively. It was observed that Si eutectic phase and Fe-bearing IMPs formed along the primary Al phase boundary, however, some coarse Fe-bearing IMPs are formed within the primary Al phases; it may be assumed that these IMPs are formed before the primary Al phases are solidified.

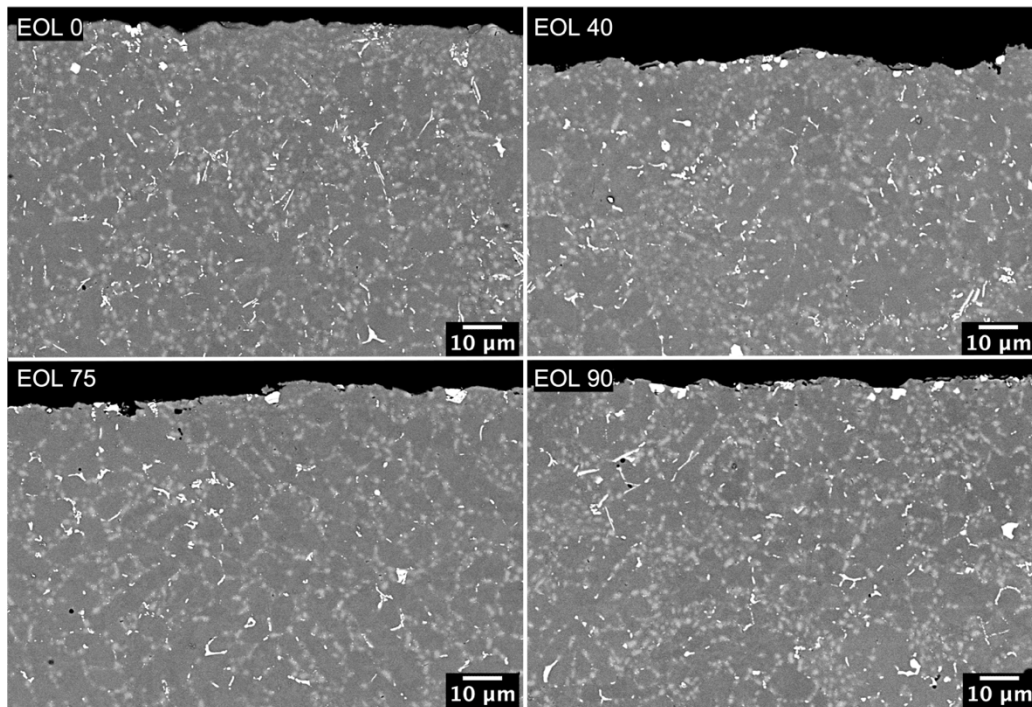


Figure 5.3: BSE images of each EOL alloy, skin region

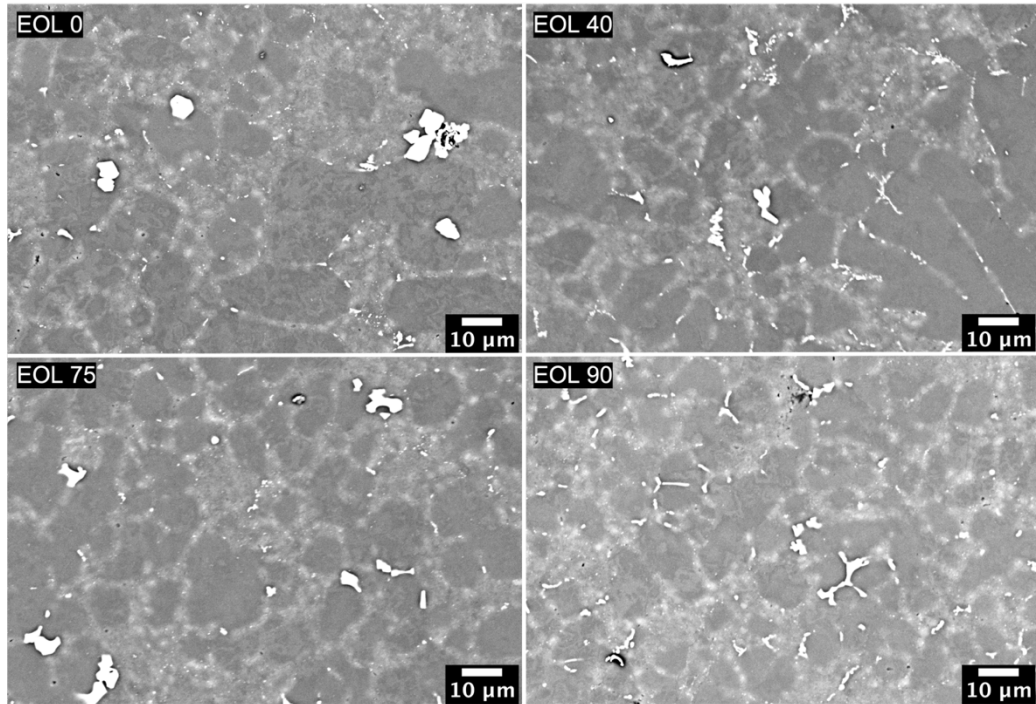


Figure 5.4: BSE images of each EOL alloy, core region

The area fraction of IMPs, Si eutectic phase, and primary Al phase in the skin and core, as determined from image analysis, are tabulated in Table 5.2. The error bars represent a 95% confidence interval associated with average value reported for the acquired data set in each case.

Table 5.2: Microstructure characteristics obtained by SEM-BSE images

Alloy	Skin			Core		
	Primary Al	Si eutectic	IMP	Primary Al	Si eutectic	IMP
EOL 0	84.0 ± 1.6	14.7 ± 1.5	1.3 ± 0.3	87.4 ± 2.8	10.8 ± 2.5	1.8 ± 0.4
EOL 40	83.5 ± 4.1	14.9 ± 4.0	1.6 ± 0.2	86.5 ± 1.1	12.1 ± 1.0	1.4 ± 0.5
EOL 75	83.5 ± 1.8	15.2 ± 1.8	1.3 ± 0.1	85.1 ± 1.2	12.8 ± 1.0	2.1 ± 0.9
EOL 90	79.5 ± 3.1	18.7 ± 2.9	1.8 ± 0.2	83.3 ± 1.8	14.5 ± 1.5	2.2 ± 0.9

All EOL alloys contained comparable fraction of primary Al phase and Si eutectic within the skin region, although a higher IMPs fraction was observed on some secondary alloys.

The core region contained much larger primary Al phases compared to the skin region which was predictable from a HPDC solidification perspective. It was also evident that the core regions contained less Si eutectic phase when compared to the skin region.

From the starting microstructure characterization, several summarizing observations were extracted:

1. A higher fraction of coarse IMPs in the skin was observed in the secondary EOL alloys, relative to that observed in the primary (EOL 0) alloy.
2. A smaller primary Al cell size in the skin, relative to the core, was observed in each EOL alloy.
3. A smaller fraction of Si eutectic phase in the skin, relative to core, was observed in each EOL alloy.

4. A direct correlation between the EOL contents and microstructure characteristics such as primary Al size cell, fraction of Si eutectic phase, fraction of IMPs was not observed on both skin and core region.

Based on the electrochemical polarization and corrosion visualization measurements presented in Section 5.2, the major difference in localized corrosion susceptibility occurred between the primary and the secondary alloys, regardless of the EOL content. For this reason, the skin microstructure of EOL 0 (primary alloy) and EOL 40 (representing secondary alloys) was further examined using SEM-EDS.

Figure 5.5 and Table 5.3 demonstrate the SEM-EDS spot analysis and mapping results on EOL 0. The mapping revealed that IMPs observed on EOL 0 contained both Fe and Mn and a high Mn content was also detected. Figure 5.6 and Table 5.4 demonstrate the SEM-EDS spot analysis and mapping results on EOL 40. IMPs observed on EOL 40 had similar compositional profile with respect to ones observed on EOL 0. Some regions consisted of Mg and Zn were observed at the surface of EOL 40, which aligned with the result obtained by XPS analysis (Section 5.3).

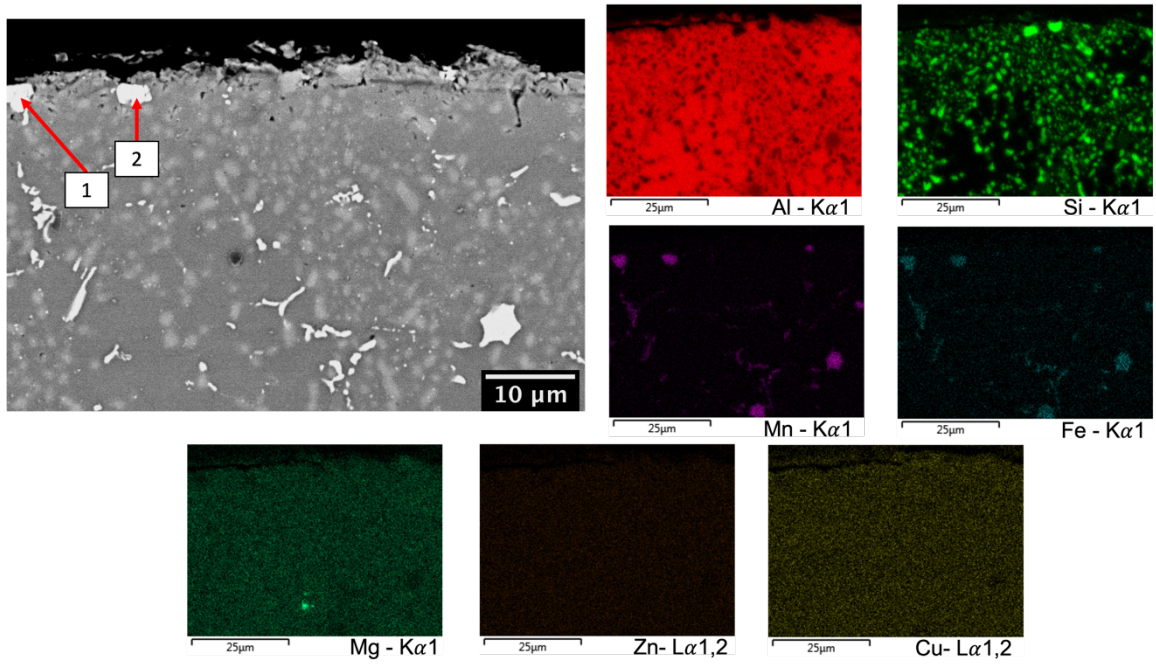


Figure 5.5: EDS mapping of EOL 0, skin region

Table 5.3: Elemental composition of spot analysis (wt%)

Spot number	Al	Si	Mn	Fe
1	61.1 ± 1.6	12.3 ± 0.8	21.1 ± 1.5	5.5 ± 1.3
2	62.9 ± 1.5	10.5 ± 0.8	21.9 ± 1.4	4.5 ± 1.2

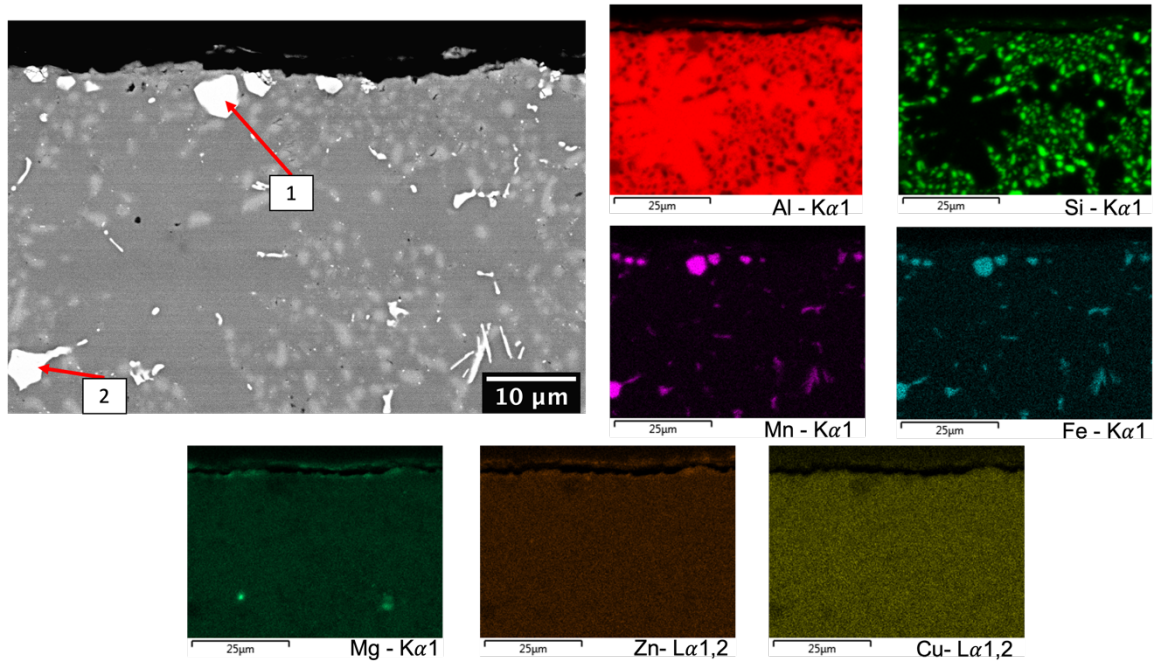


Figure 5.6: EDS mapping of EOL 40, skin region

Table 5.4: Elemental composition of spot analysis (wt%)

Spot number	Al	Si	Mn	Fe
1	59.9 ± 0.2	11.3 ± 0.1	22.8 ± 0.2	5.3 ± 0.1
2	62.2 ± 0.2	11.0 ± 0.1	20.7 ± 0.2	5.7 ± 0.1

5.2 Electrochemical Polarization Measurements

Cyclic potentiodynamic anodic polarization was conducted on each EOL alloy, in both the skin and core regions. Representative cyclic polarization curves of each EOL alloy on skin and core region are illustrated in Figure 5.7 and Figure 5.8, respectively. Average value with 95% confidence intervals of breakdown potential (E_b), repassivation

potential (E_r), and ΔV ($E_b - E_r$) for each EOL alloy at skin and core regions are shown in Table 5.5 and Table 5.6, respectively. All replicate dataset is included in the Appendix.

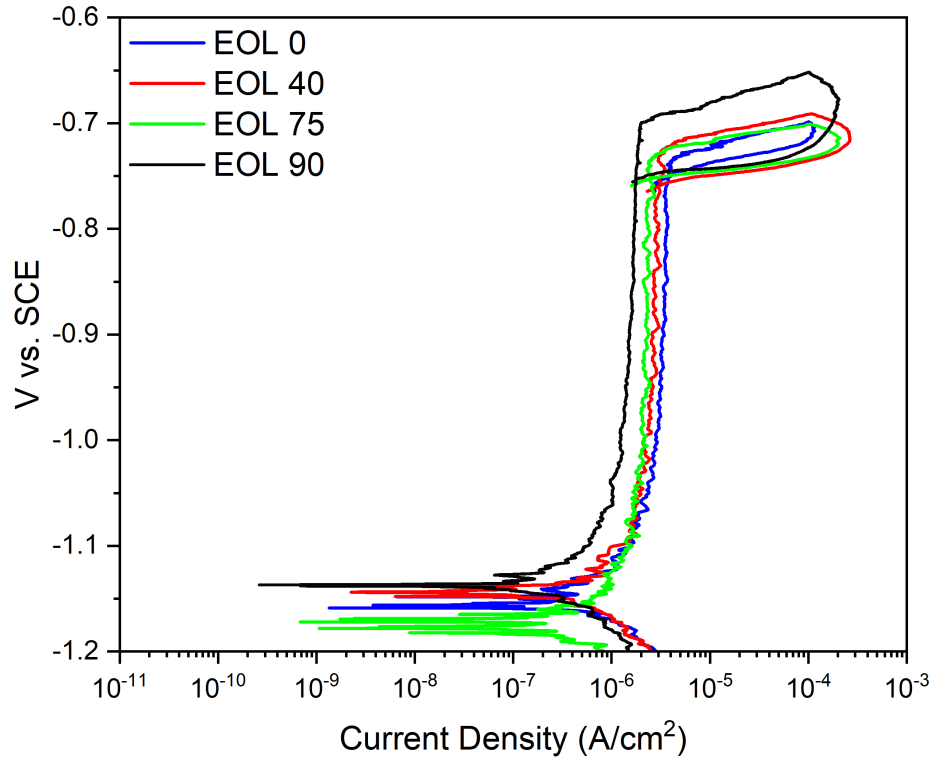


Figure 5.7: Representative cyclic polarization curves of each EOL alloy, skin region

Table 5.5: Average values of breakdown potential (E_b), repassivation potential (E_r), and ΔV ($E_b - E_r$) with 95% confidence intervals, skin region

	E_b (mV)	E_r (mV)	ΔV (mV)
EOL 0	-760 ± 14	-772 ± 18	12 ± 6
EOL 40	-718 ± 15	-742 ± 6	24 ± 13
EOL 75	-748 ± 2	-772 ± 8	24 ± 10
EOL 90	-744 ± 11	-781 ± 16	37 ± 5

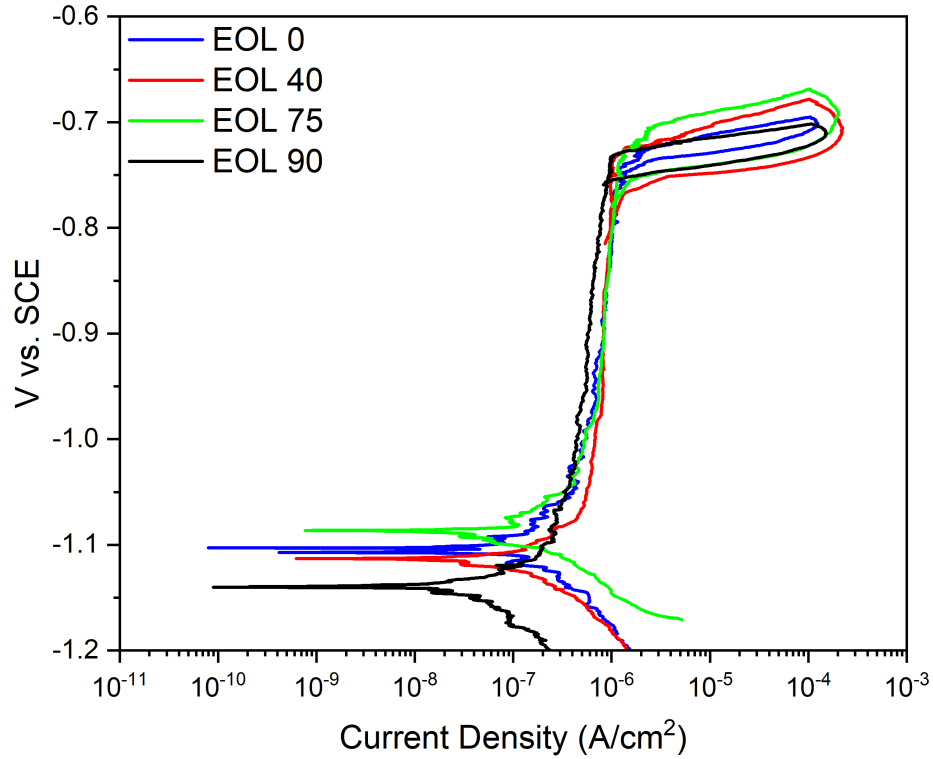


Figure 5.8: Representative cyclic polarization curves of each EOL alloy, core region

Table 5.6: Average values of breakdown potential (E_b), repassivation potential (E_r), and ΔV ($E_b - E_r$) with 95% confidence intervals, core region

	E_b (mV)	E_r (mV)	ΔV (mV)
EOL 0	-739 ± 5	-759 ± 4	17 ± 6
EOL 40	-727 ± 8	-790 ± 12	63 ± 16
EOL 75	-761 ± 16	-796 ± 15	35 ± 12
EOL 90	-744 ± 5	-781 ± 15	41 ± 20

No direct relationship between a trend in the E_b , E_r values and the EOL content was observed on the skin or the core surfaces. However, the ΔV values were different between the primary alloy (EOL 0) and secondary alloys, regardless of the EOL content.

The difference was more pronounced for the skin surfaces than the core surfaces. EOL 0 demonstrated the smallest value of ΔV . The similar potentiodynamic anodic polarization response exhibited by the skin and core surface of each EOL alloy suggested that any difference in microstructure between the two does not affect localized corrosion susceptibility. Major differences between the skin and the core, as revealed by microscopy include the primary Al cell size and Si eutectic phase fraction. It followed then that neither of the two differences affected localized corrosion susceptibility. Accordingly, localized corrosion susceptibility of the core surface was not investigated further; focus was placed solely on the skin surface. This was justified that any localized corrosion initiation observed in service, would initiate on the skin surface.

Cross-sectional images of EOL alloys after potentiostatic anodic polarization are shown in Figure 5.9. It was observed that All EOL alloys experienced inter-dendritic attack along the primary Al phase boundary. No difference in propagation corrosion mode was observed throughout all EOL alloys.

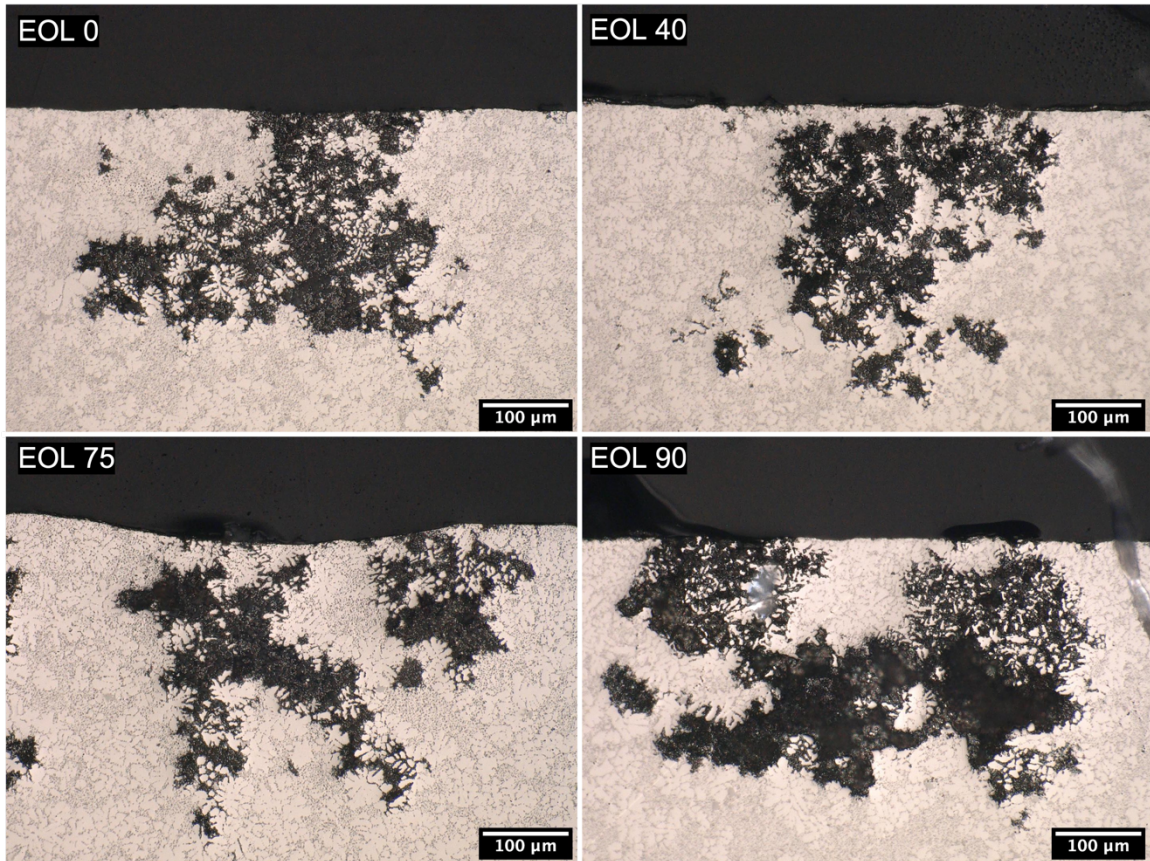


Figure 5.9: Cross sectional images of post potentiostatic anodic polarization, obtained by LOM, polarization measurement conducted by Darren Feenstra

The potential transients of each EOL alloy recorded during galvanostatic anodic polarization ($+1 \text{ mA/cm}^2$) are shown Figure 5.10. The replicate dataset of the potential transients is included in the Appendix.

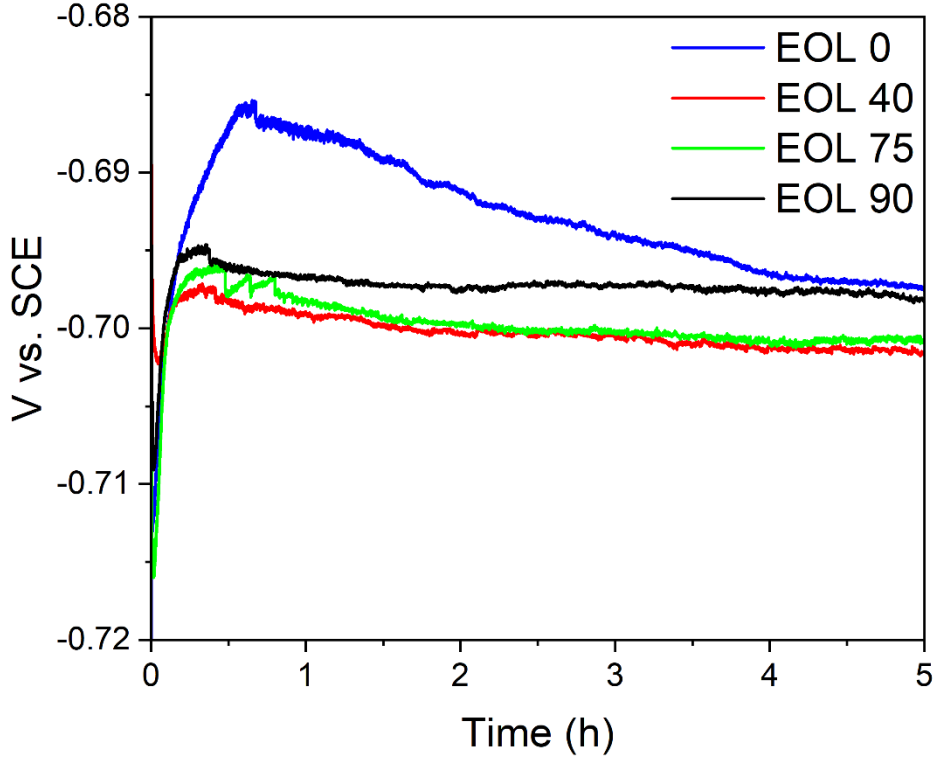


Figure 5.10: Potential transient of each EOL alloy during galvanostatic anodic polarization (+ 1 mA/cm² for 5 h)

The potential transient for each EOL alloy exhibited similar features; this includes an initial rise in potential to a local maximum value before a slow decay towards a steady state value. The local maximum potential attained was highest (most noble) for EOL 0, whereas a similar value was observed for the secondary alloys with no apparent effect of EOL content. The time to attain this local maximum potential was also longest for EOL 0. A shorter and similar time was exhibited by all secondary alloys. The maximum potential, and associated time to attain it was interpreted as indicating a passive film breakdown event (localized corrosion initiation). It followed then that EOL 0 exhibited the lowest

susceptibility to breakdown. The trend towards a similar steady state potential indicated that all alloys exhibited a similar susceptibility to corrosion after the breakdown event. Cross-sectional images of EOL alloys after galvanostatic anodic polarization are shown in Figure 5.11. Similar observations from post potentiostatic anodic polarization samples were demonstrated; no difference in corrosion mode was observed throughout all EOL alloys.

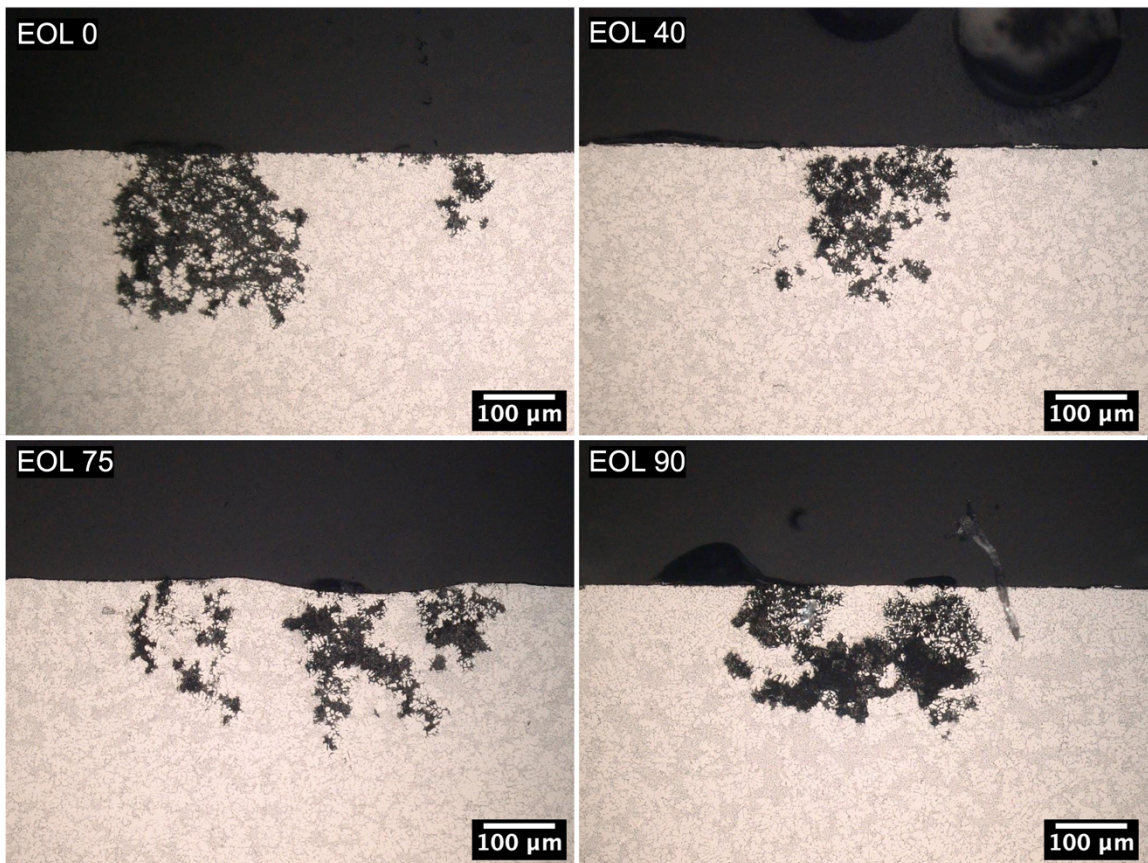


Figure 5.11: Cross sectional images of post galvanostatic anodic polarization

Figure 5.12 illustrates the metastable current density transient curves of EOL 0 and EOL 40. The indications of metastable localized corrosion initiations were marked with

arrows. The replicate dataset of the metastable current transients is included in the Appendix. EOL 0 exhibited no indication of metastable localized corrosion initiation while EOL 40 demonstrated a few indications; EOL 40 had a higher susceptibility to metastable localized corrosion initiation. It also should be noted that the higher current transient on EOL 0 was observed with no indication of metastable localized corrosion. This may be explained by the higher resistance to the metastable localized corrosion initiations exhibited by EOL 0.

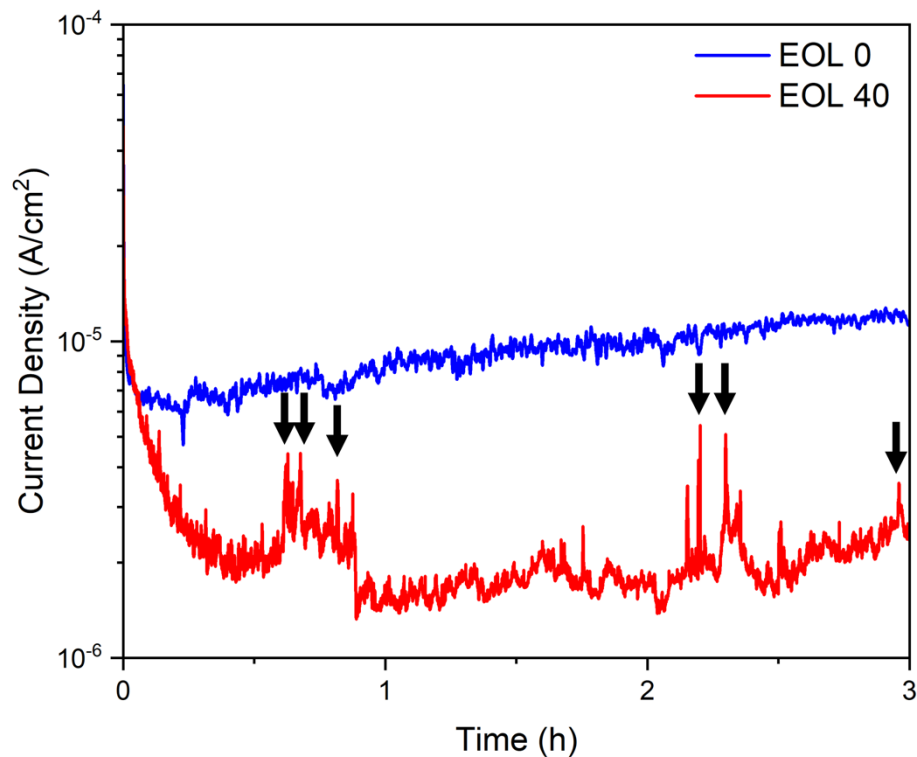
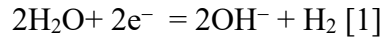


Figure 5.12: Current density transients of EOL 0 and EOL 40 with an applied metastable potential (20 mV below E_b)

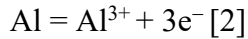
5.3 Corrosion Visualization Experiment

Images of agar gel electrolyte-covered EOL alloy samples at the beginning and after 4 h of exposure are shown in Figure 5.13 and Figure 5.14, respectively. The cathodic reaction was expected to be as follows:



At the cathodic regions (blue colour), hydroxide ions are generated where agar gel and the alloy are in contact (Equation [1]).

The reactions of Al dissolution and H^+ ions formation were as follows:



Since the anodic dissolution of the Al alloy produces H^+ ions, this will decrease the pH at dissolution site (Equation [2] and [3]). The decrease in pH was manifested by a red colouration in gel upon reaction of the H^+ ions with the universal indicator. As shown in Figure 5.14, many anodic sites were observed on the secondary alloys after 4 h of exposure. In contrast, EOL 0 exhibited just a single anodic site after 4 h exposure. This indicates that the secondary alloys are more prone to localized corrosion initiation. Qualitatively speaking, there was no obvious trend between the number of initiation sites and the EOL content in the secondary alloys.

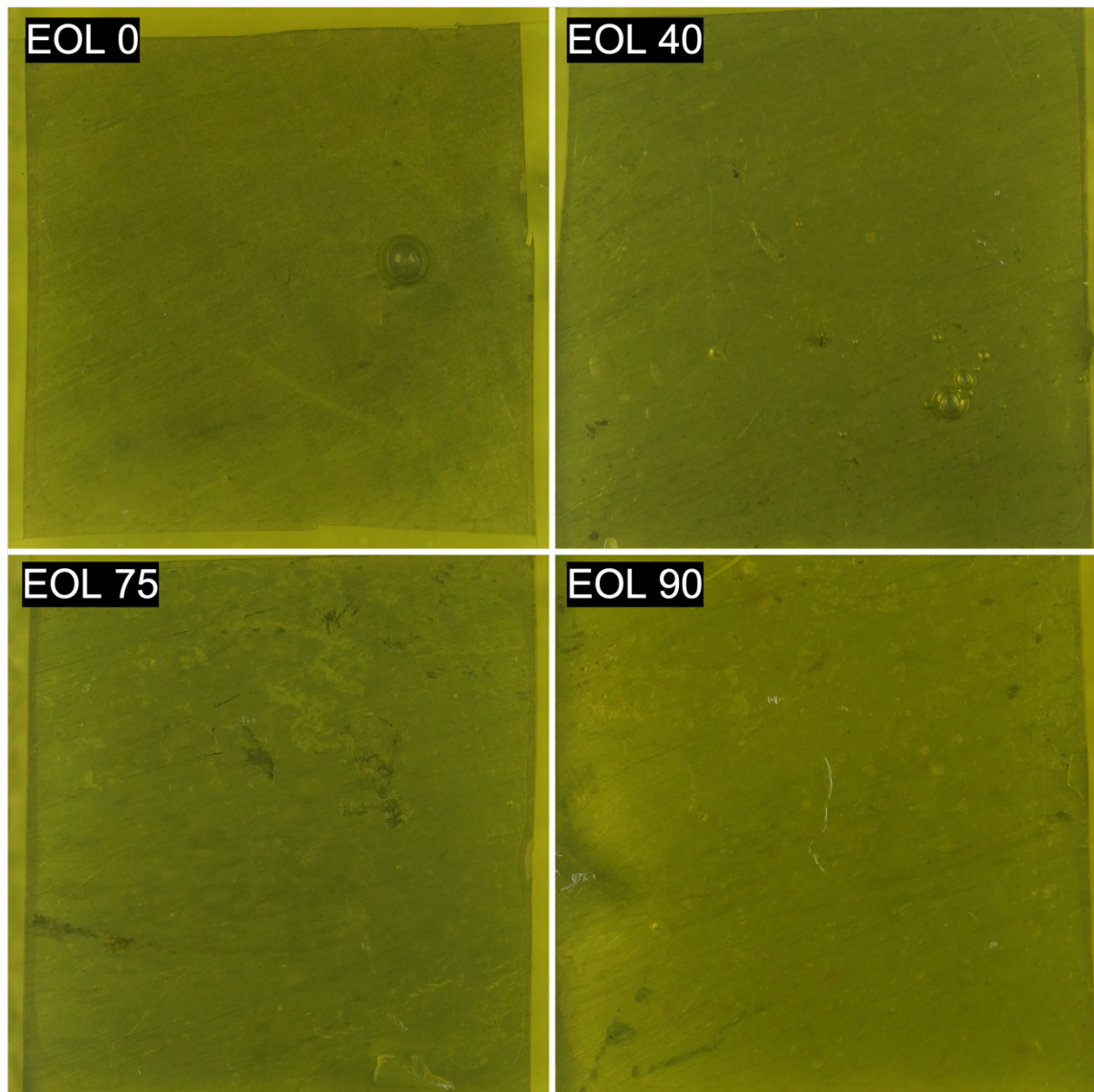


Figure 5.13: Images of agar gel electrolytes at the beginning of the experiment (0 h)

¥

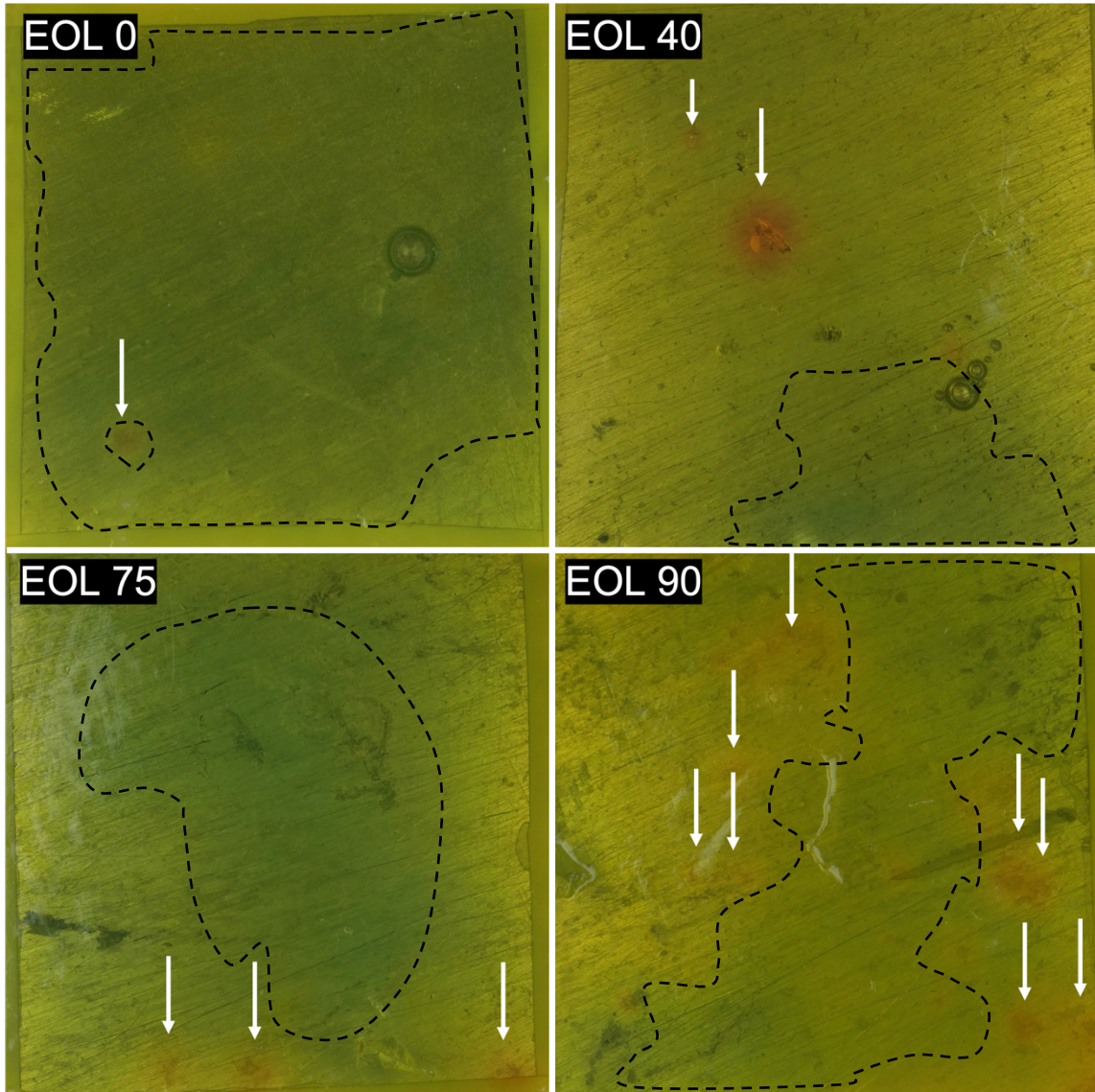


Figure 5.14: Images of agar gel electrolytes after 4 h of the exposure, dotted line demarks the cathodic region (blue colour)

5.4 X-Ray Photoelectron Spectroscopy

Since both the electrochemical polarization and corrosion visualization measurements show that the major difference in localized corrosion susceptibility was between the

primary alloy and secondary alloys, regardless of the EOL content. Thus, the XPS analysis of passive films formed during potentiostatic anodic polarization was limited to EOL 0 (primary alloy) and the EOL 40 (representing the secondary alloys).

The O concentration depth profile is shown with a respect to sputter time in Figure 5.15. No attempt was made to correlate the sputtering time with distance given the lack of an appropriate standard to calibrate the sputtering time in this way. The location of passive film/metal interface is conventionally located at the sputtering time (distance) at which the O concentration profile drops to 50% of difference between maximum and minimum concentration value measured (full width half maximum) [71] [72]. Following this convention, the film/metal interface was located at 2.6 minutes and 1.6 minutes for EOL 0 and EOL 40, respectively. This time difference may be indicative of differences in the passive film thickness. Regardless, the main reason to locate the film/metal interface was to help interpret enrichment/depletion of alloying elements in the film relative to the metal.

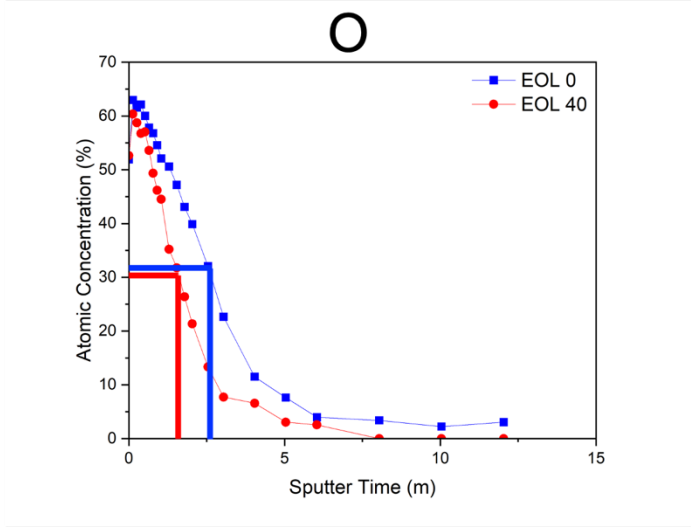


Figure 5.15: Concentration depth profile for O as a function for sputter time, EOL 0 and EOL 40; Solid lines demark the passive film/metal interface.

Other elements detected on the passive surface, for which concentration depth profiles were acquired, include Al, Si, Mn and Cu along with O for both alloys and additional Zn and Mg for EOL 40. A concentration depth profile for each element in both alloys is shown with a respect to sputter time in Figure 5.16. The atomic concentration of Al and Si within the passive films and metal region were comparable between EOL 0 and EOL 40. Cu and Mn signals were detected on EOL 0 and EOL 40, both within the passive film and metal region. EOL 0, however, exhibited no signal of Mg and Zn, while both were detected within the passive film in EOL 40, indicating that Mg and Zn may be co-existing within the passive film and metal region of EOL 40. It was also notable that Mg was still detected at the location of passive film/metal interface. Zn was detected within the passive film region, then completely depleted from the interface to the sputtering time of approximately 10 minutes. It should be noted that Mg was also detected at the location of approximately 10 minutes of the sputtering time. This may be significant evidence that

Mg-Zn phase may also co-exist within the metal region of EOL 40, which aligned with the result observed on SEM-EDS in Section 5.1.

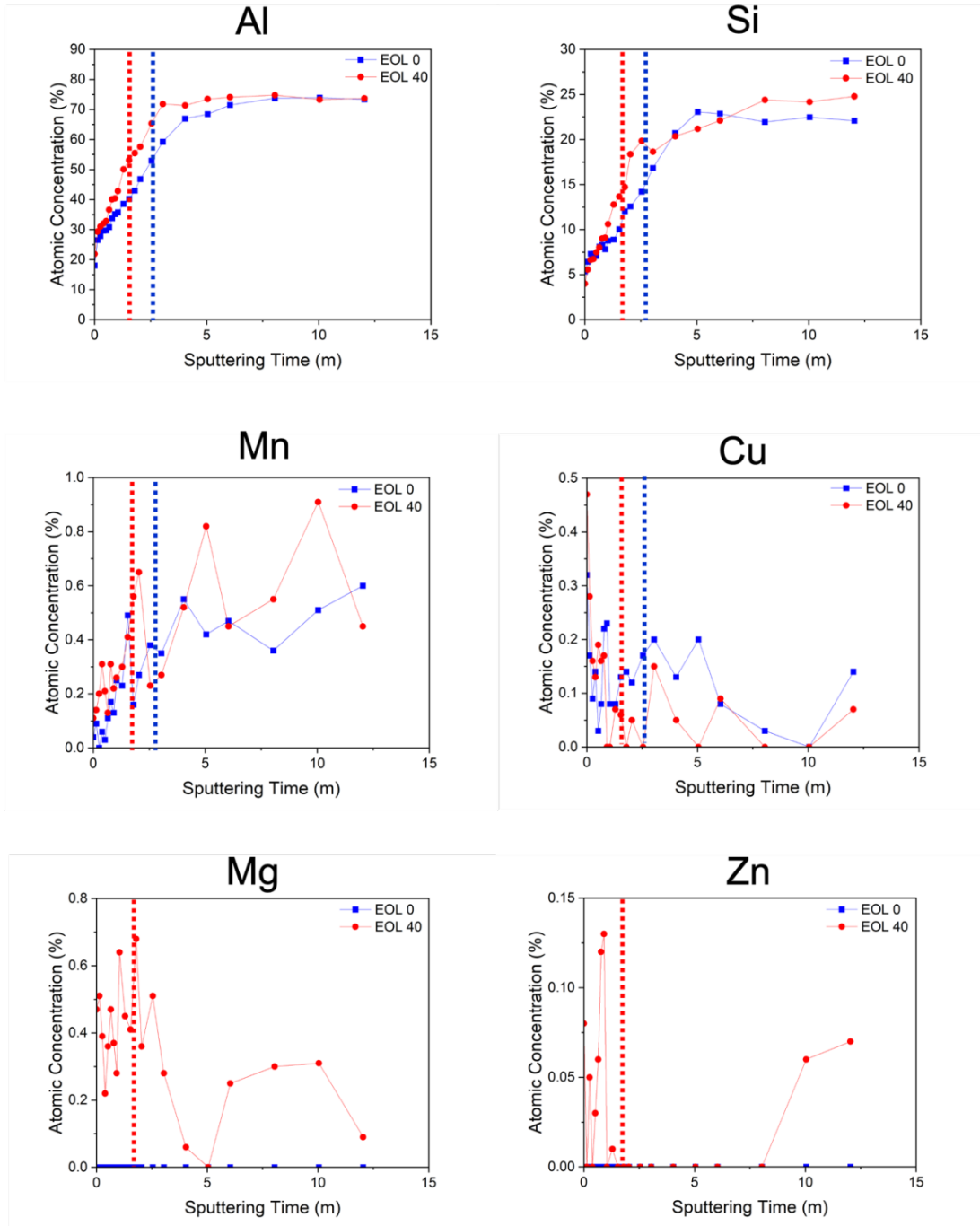


Figure 5.16: Atomic concentration of detected element as a function of sputter time during depth profiling, EOL 0 and EOL 40. Dotted line indicating passive film/metal interface of each EOL alloy

Chapter 6: Discussion

It was observed that secondary alloys were more prone to localized corrosion than the primary alloy, regardless of the EOL content; the same trend was observed on both skin and core region. Similar localized corrosion mode was also observed regardless of the EOL content, which involved inter-dendritic corrosion. It should be mentioned that all polarization measurements and corrosion visualization experiments suggested the difference in initiation stage between the primary and secondary alloys. Table 6.1 summarizes all electrochemical characteristics of the EOL alloys with a focus on EOL 0 and EOL 40 (representing the secondary alloys). Considering E_b , E_r , and ΔV obtained by cyclic polarization, EOL 0 exhibited the lowest E_b value; EOL 0 may breakdown at lower potential level compared to secondary alloys. However, the potential level may not reflect to the localized corrosion rate or propensity. As previously mentioned, ΔV value is a measurement that can be used to evaluate the repassivation tendency. With EOL 0 having a smallest ΔV value, EOL 0 had a greater tendency to repassivate in comparison to secondary alloys. Since the corrosion mode is localized in nature, both breakdown and repassivation tendency are critical factors affecting localized corrosion susceptibility. In fact, galvanostatic anodic polarization confirmed that the secondary alloys were more prone to localized corrosion initiation than the primary alloy. Result from agar gel experiment demonstrated the susceptibility of localized corrosion initiation. By combining those justifications, it can be concluded that EOL 0 had a lower localized corrosion susceptibility than secondary alloys, on account of being less prone to localized breakdown events.

Table 6.1: Electrochemical characteristics of EOL 0 and EOL 40

Alloy	E_b (mV)	E_r (mV)	ΔV (mV)	Breakdown Time (GS) (h)
EOL 0	-760 ± 14	-772 ± 18	12 ± 6	0.97 ± 0.08
EOL 40	-718 ± 15	-742 ± 6	24 ± 13	0.33 ± 0.17

Table 6.2 summarizes all microstructure characteristics of the EOL alloys with a focus on EOL 0 and EOL 40, observed at the skin region. While the primary Al phase cell size and IMP fraction observed at the skin region of EOL 0 was determined to be smaller than observed on EOL 40, the Si eutectic fraction was found to be comparable. It was, however, noted that IMP fraction observed on EOL 0 and EOL 40 was somewhat distinguishable. IMPs at the skin region heavily influence the localized corrosion initiation through micro-galvanic effect between primary Al phase and Fe-containing IMPs [11]. It was also critical that the Mg-Zn feature detected by XPS and SEM-EDS analysis was only observed on EOL 40.

Table 6.2: Microstructure characteristic of EOL 0 and EOL 40 (skin region)

Alloy	Primary Al cell size (μm)	Si eutectic area fraction (%)	IMP area fraction (%)	Fe- containing IMP	Mg-Zn feature
EOL 0	7.5 ± 0.7	14.7 ± 1.5	1.23 ± 0.3	Yes	No
EOL 40	12.9 ± 0.9	14.9 ± 4.0	1.60 ± 0.2	Yes	Yes

It was still, however, uncertain what the critical factors were that render secondary alloys to be more prone to localized corrosion initiation. Three working theories can be deduced from the differences in the microstructure reported in Table 6.2:

1. Distribution and chemistry of Fe-bearing IMPs (Mn and Cu impurity effect)

2. Primary Al phase cell size and Si eutectic distribution (Ti structure refiner effect)
3. Mg-Zn rich zone/phase at surface (Zn impurity effect)

Microstructure analysis with BSE images confirmed that the secondary alloys contained a higher fraction of coarse IMPs within the skin. This could affect the localized corrosion initiation since Fe-containing IMPs are cathodic relative to Al phase, promoting a higher probability of micro-galvanic corrosion initiation [7] [62] [73] [74]. While a higher fraction of IMPs was observed on EOL 40, the chemistry of IMPs observed on EOL 0 and EOL 40 were similar. As previously mentioned in Chapter 2, Mn content within Fe-containing IMPs had a significant role on the electrochemical characteristic; Mn suppresses the cathodic effect of Fe-containing IMPs [61]. The presence of impurity elements such as Cu, however, may be introduced to IMPs which can modify the electrochemical characteristics. Cu-containing IMPs such as θ -Al₂Cu and ω -Al₇Cu₂Fe are more noble than α -Al₁₅(Fe,Mn)₃Si₂, and β -Al₅FeSi [12]. Typically, Cu-containing IMPs were not observed in A365 since the Cu content was kept less than 0.03 wt% [68], however, the secondary alloys contained 0.07 wt%. Cu-containing IMPs were not observed in the SEM-EDS examination, indicating that more exhaustive SEM-EDS characterization of the IMPs and subsequent characterization with X-ray diffraction (XRD) should be suitable to confirm the presence of Cu-bearing IMPs.

The size of the primary Al phase in Al alloy castings can affect localized corrosion susceptibility in several ways. Corrosion of Al alloy castings with low alloying element content such as the 1xx.x series can be improved with coarse primary Al phase size [75]. This can be due to the formation of a relatively homogenous (in composition) primary Al

phase; micro-galvanic corrosion is minimized due to absent of secondary and eutectic phases. In contrast, the effect of the primary Al phase size on corrosion becomes more complex for Al alloy castings with high alloying element content such as 3xx.x series. When considering corrosion propagation mode such as inter-dendritic corrosion, the corrosion propagation may be heavily influenced by the primary Al cell size. Dendrite refinement agent such as TiB_2 is typically added to reduce the primary Al cell size; this was done to induce more homogenous Al dendrite nucleation. It can be anticipated that the Si eutectic network and IMPs distributions may be influenced by those dendrite refinement. In fact, image analysis of the BSE images of the microstructure in cross-section revealed a notable difference in the Si eutectic fraction observed in skin and core regions. It was originally considered that a higher Si eutectic content would increase the localized corrosion susceptibility due to a high driving force promoted by cathodic effect of Si eutectic phases, however, cyclic potentiodynamic anodic polarization measurements did not reveal this to be the case. Thus, it can be concluded that Si eutectic content and primary Al cell size itself within A365 system was not responsible for the increased localized corrosion susceptibility exhibited by the secondary alloys. In conclusion, the effect of TiB_2 addition on localized corrosion susceptibility was not fully confirmed. However, Al eutectic phase may serve as the primary sites for anodic dissolution. Further investigation on Al eutectic phase is imperative to fully substantiate the effect of primary Al cell size.

Co-enrichment of Mg and Zn at the surface of EOL 40, and associated incorporation into the passive film that forms, was identified by SEM-EDS and XPS examinations.

Considering Mg is more active than Al and Zn in forming an oxide film [76], the co-enrichment of Mg at the surface was likely the source for the section of MgO in the passive film. Such incorporation has been shown to compromise passive film stability [77] [78]. However, since the Mg content in the primary alloy and secondary alloy were almost identical, other factors within secondary alloy must have caused the Mg enrichment at the surface. The likely factor was the elevated Zn content in the secondary alloys. Therefore, understanding an effect of Zn on the passive film, metal region, and its interaction with Mg was essential. The most common Mg-Zn-based precipitates observed in cast Al alloys is MgZn₂, which is observed in 7xx.x series and the presence of MgZn₂ precipitates has been rarely reported in 3xx.x series. Ikeuba et al. [77] studied the galvanic corrosion behaviour of Al and MgZn₂ particles and oxide film formed on MgZn₂ particle during NaCl immersion test. It was mentioned that MgO/Mg(OH)₂ layer was formed on MgO/Mg(OH)₂/ZnO layer, attributing a higher activity of Mg and the preferential formation of MgO. Recent research of Zhou et al. [78] has shown the effect of Mg-rich zone on the passive film stability within Al-Zn-Mg-Cu alloy. They claimed that Mg-rich zones can be formed when η (MgZn₂ or MgCu₂) phases were present. Those Mg-rich zones created the inconsistency within the Al oxide passive film by forming localized MgO sites. It was demonstrated that this inconsistency within the Al oxide passive film created the lattice vacancies, allowing Cl⁻ ions to be penetrated to induce passive film breakdown, as shown in Figure 6.1.

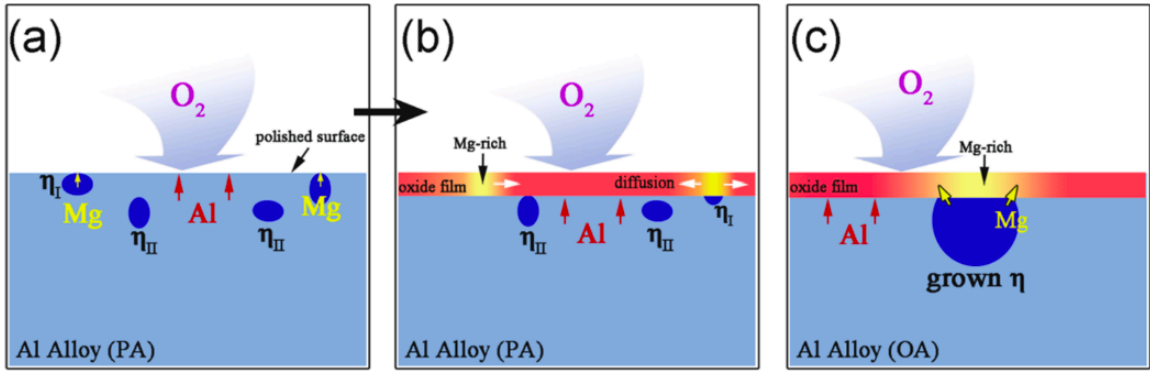


Figure 6.1: Illustration of the effect of Mg-rich zone on the passive film stability [78]

The dealloying of Mg from η phases was also highly anticipated; this would continuously create the MgO-rich zone on the passive film. This phenomenon can occur if Mg-bearing phases were enriched at the surface, yet Zn was the most prone to affect the enrichment of Mg based on SEM-EDS analysis, as well as XPS depth profiling result.

It is necessary to verify this theory with Al-Si alloys. Considering the Zn content in secondary alloy ($\cong 0.02$ wt%), there is still a lack of understanding regarding the feasibility of $Mg(Zn, Cu, Al)_2$ formation. To confirm the presence of $MgZn_2$ phase, as well as Mg or/and Zn rich zones, alternative technique such as XRD or further investigation with SEM-EDS should be employed in any future work.

Chapter 7: Conclusion and Future Work

Implementation of EOL material content when making near net shaped A365-T7 alloy castings using the HVHPDC process is requisite for automotive application as the demand of sustainable structural Al alloy castings is significantly increasing. The effect of EOL material content contained in HVHPDC A365-T7 on localized corrosion susceptibility was investigated through various electrochemical polarization measurements, corrosion visualization experiment, and microstructure characterizations. The major conclusions extracted from this research are summarized below:

1. Throughout all EOL alloy, some distinguishable microstructure features between the skin and core were observed; primary Al cell size within the skin was found to be smaller than that observed in the core. On the other hand, Si eutectic fraction observed on skin region was larger than observed on core region. EOL 0 contained smaller primary Al cell size than all secondary alloys at skin region, indicating that structure refinement was properly activated. The cast quality was not affected by the amount of EOL content introduced. Although IMPs fraction of EOL 0 observed on skin region was smaller than all secondary alloy, the difference in morphology and chemistry of IMPs was not fully confirmed between EOL 0 and EOL 40.
2. Characteristic electrochemical potentials associated with localized corrosion were successfully obtained by cyclic potentiodynamic anodic polarization. Although E_b of EOL 0 was the lowest of all EOL alloys, EOL 0 exhibited the highest tendency of repassivation. Localized corrosion propagation mechanism of all EOL alloys

was found to be similar through observing the post potentiostatic anodic polarization measurements. Galvanostatic anodic polarization also confirmed the similar corrosion propagation of all EOL alloys and revealed that the primary alloy exhibited the lowest susceptibility to localized corrosion initiation. Agar gel experiment further supported that localized corrosion initiation propensity of EOL 0 was the lowest. Finally, metastable current transients indicated that EOL 40 (representing secondary alloy) had a higher susceptibility to metastable localized corrosion initiation in comparison to EOL 0.

3. A major difference between the primary alloy and the secondary alloys regarding localized corrosion susceptibility was related to the initiation stage of localized corrosion. Three working theories were identified to account for the difference in susceptibility: (i) Al-Si-Mn-Fe IMPs contribution (distribution and/or chemistry effect), (ii) structure refinement (Ti effect) , and (iii) Mg-Zn phase formation (compromised passive film effect).

The overall localized corrosion susceptibility of secondary alloys may be affected by one or a combination of those working theories. Those working theories shall be further investigated through performing microstructure and electrochemical characterization, as well as passive film stability with new cast trials, as tabulated in Table 7.1.

Table 7.1: Future work regarding the proposed working theories

Working theory	Future work
Coarse IMP Micro-Galvanic Corrosion Effect	Performing SKPFM on IMPs observed on EOL 0 and EOL 40 to obtain Volta potential to confirm the electrochemical reactivity differences (driving force for micro-galvanic corrosion).
Structure Refinement Effect	Comparing the microstructure and electrochemical characteristics of secondary alloys with an elevated addition of TiB ₂ for enhanced structure refinement effect.
Mg-Zn Phase Formation Effect	Investigating the Mg-Zn phase formation on secondary alloys through various technique such as XRD and SEM/EDS, as well as the passive film investigation through XPS analysis on primary alloy with an elevated Zn content ($\cong 0.02$ wt%)

Appendix

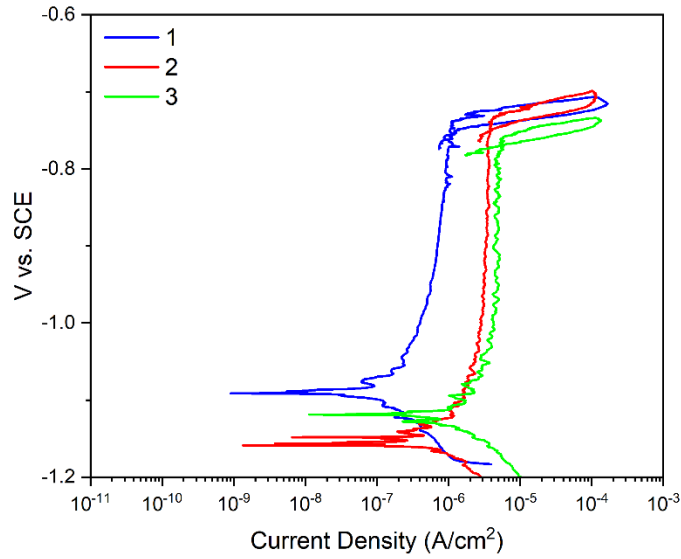


Figure A.1: Replicate dataset of cyclic potentiodynamic polarization, skin region, EOL 0

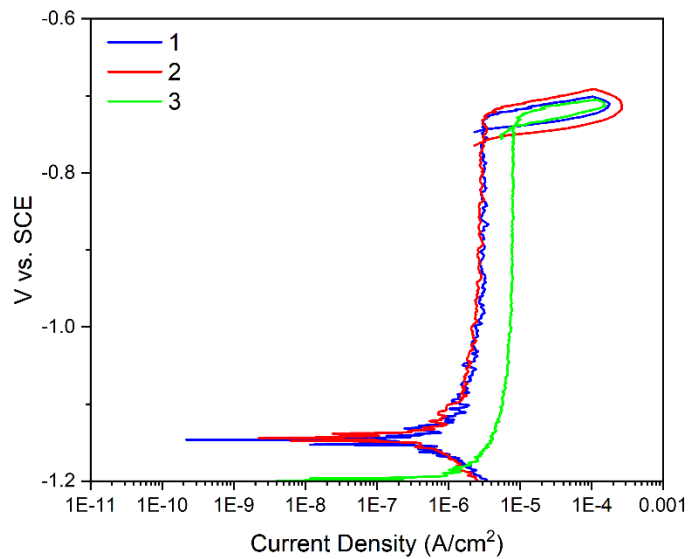


Figure A.2: Replicate dataset of cyclic potentiodynamic polarization, skin region, EOL 40

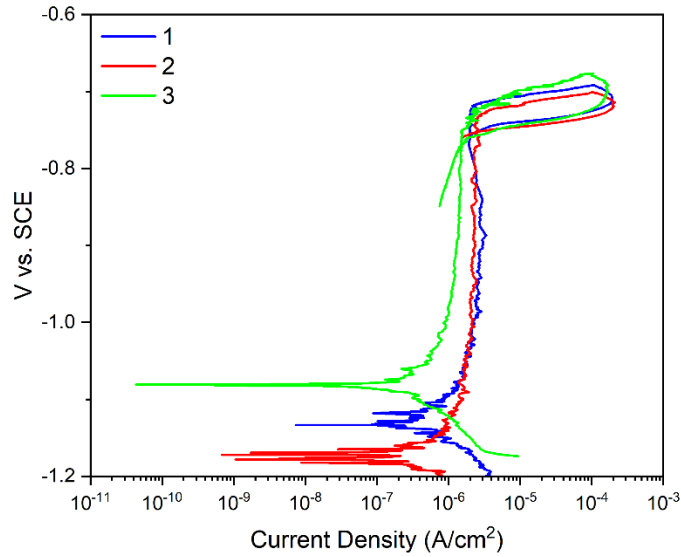


Figure A.3: Replicate dataset of cyclic potentiodynamic polarization, skin region, EOL 75

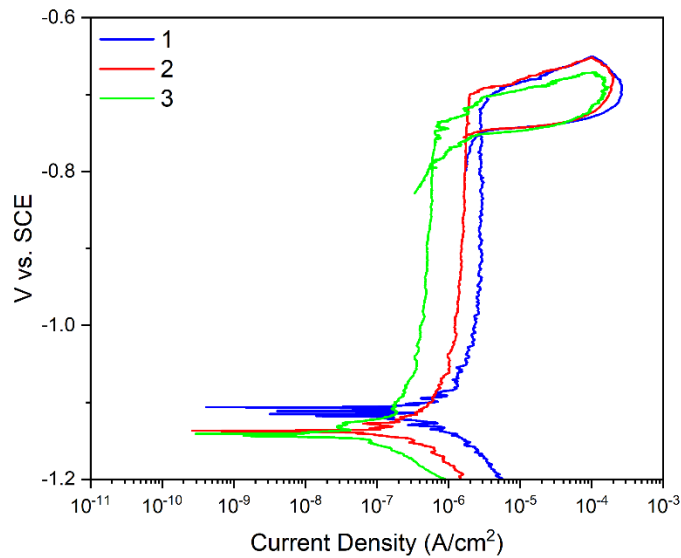


Figure A.4: Replicate dataset of cyclic potentiodynamic polarization, skin region, EOL 90

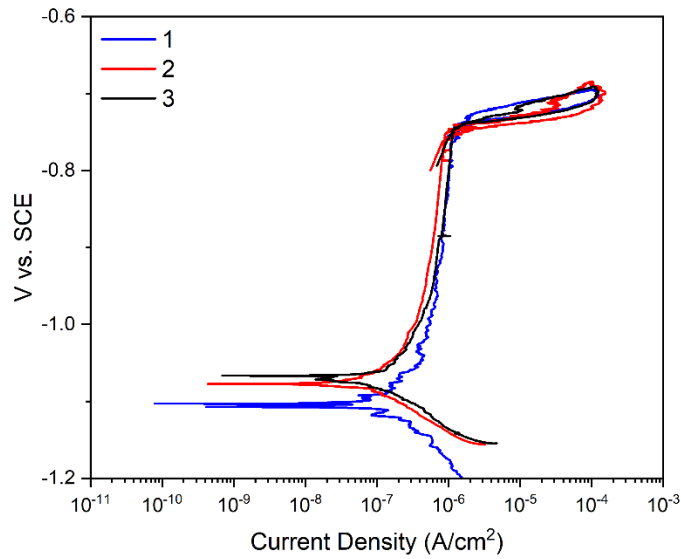


Figure A.5: Replicate dataset of cyclic potentiodynamic polarization, core region, EOL 0

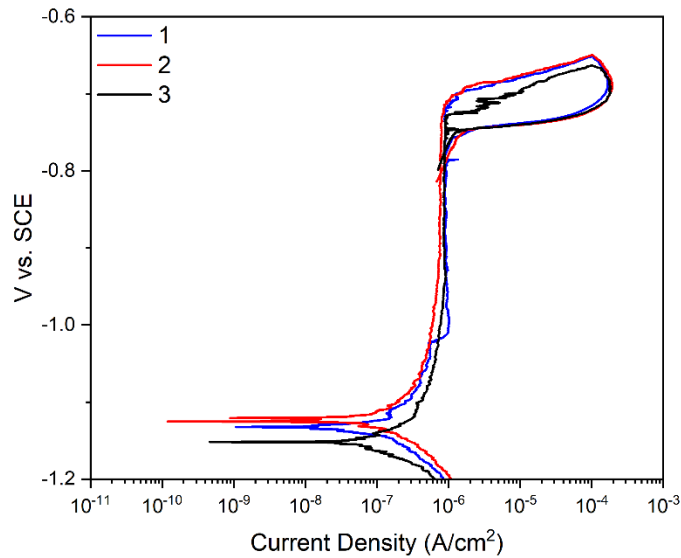


Figure A.6: Replicate dataset of cyclic potentiodynamic polarization, core region, EOL 40

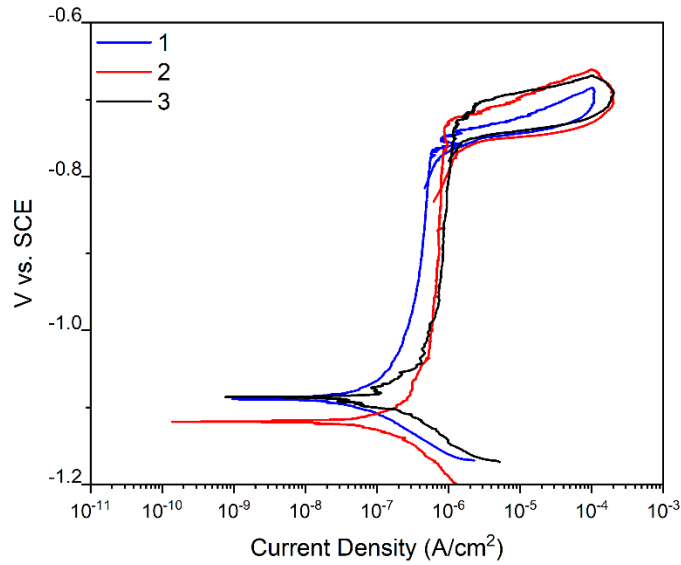


Figure A.7: Replicate dataset of cyclic potentiodynamic polarization, core region, EOL 75

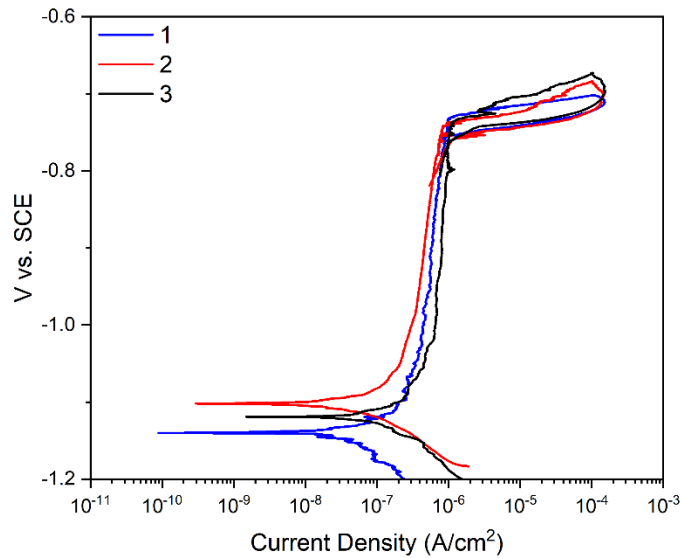


Figure A.8: Replicate dataset of cyclic potentiodynamic polarization, core region, EOL 90

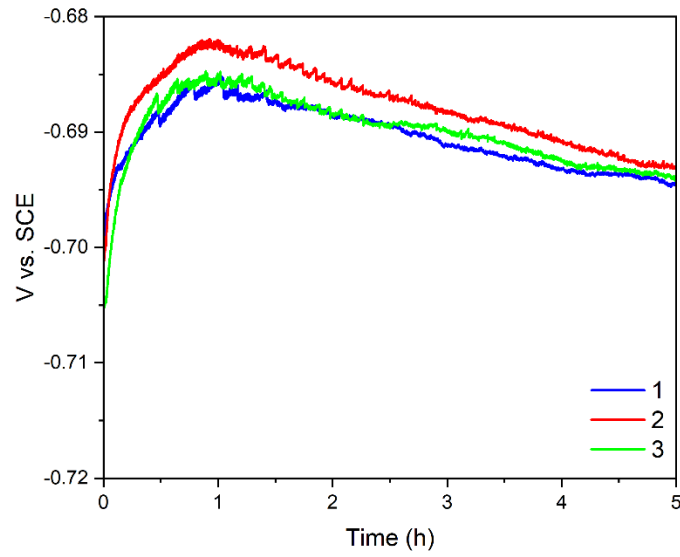


Figure A.9: Replicate dataset of galvanostatic polarization, EOL 0

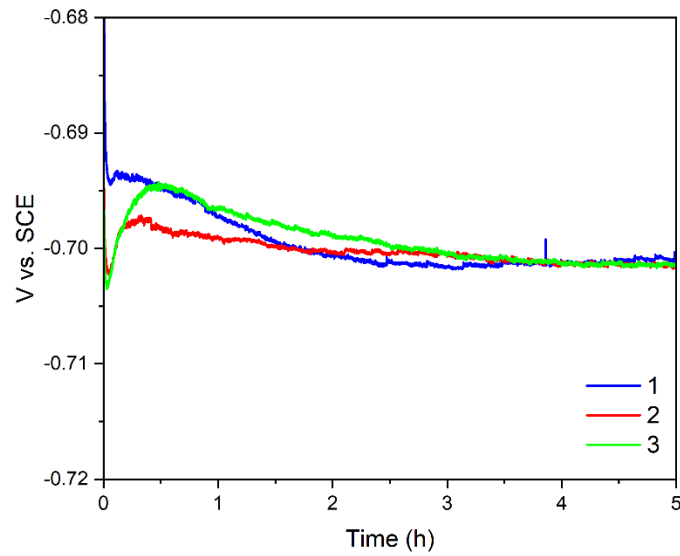


Figure A.10: Replicate dataset of galvanostatic polarization, EOL 40

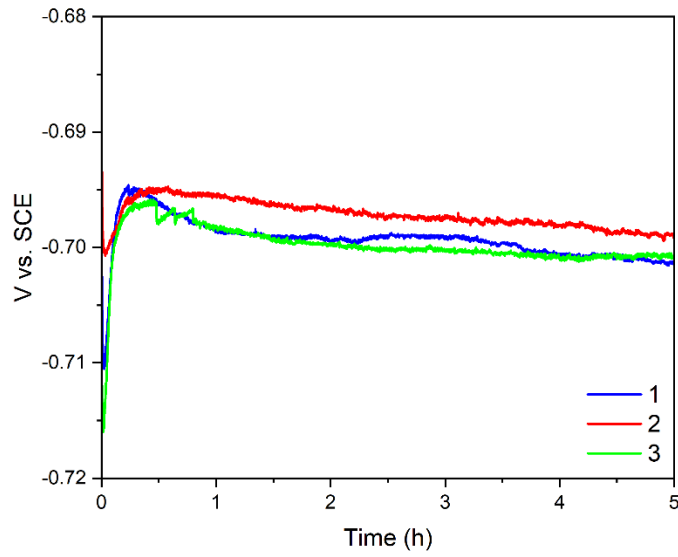


Figure A.11: Replicate dataset of galvanostatic polarization, EOL 75

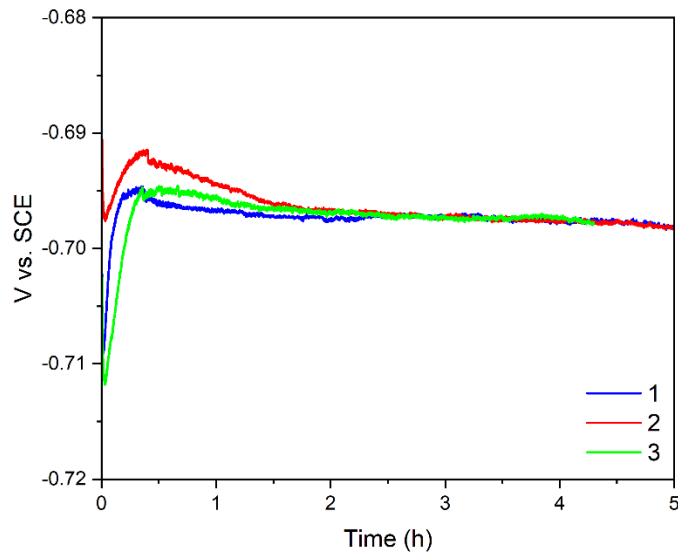


Figure A.12: Replicate dataset of galvanostatic polarization, EOL 90

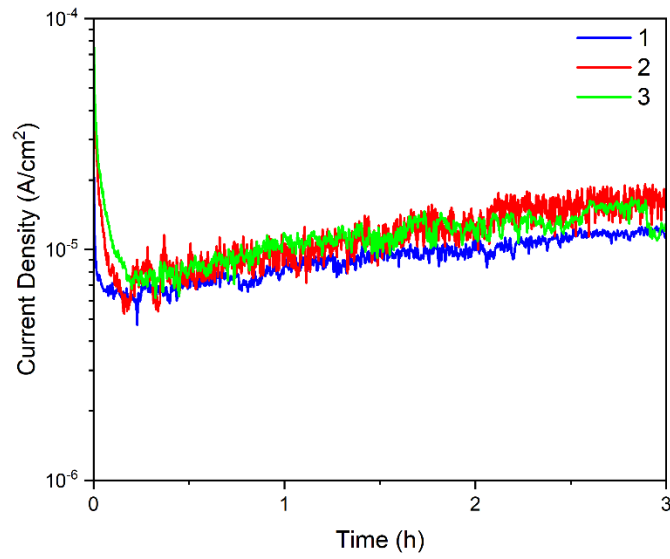


Figure A.13: Replicate dataset of current density transient for metastable localized corrosion initiation, EOL 0

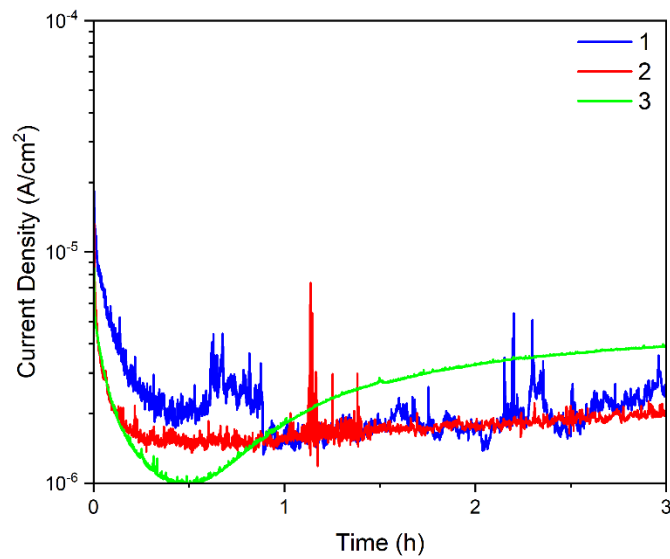


Figure A.14: Replicate dataset of current density transient for metastable localized corrosion initiation, EOL 40

Reference

- [1] L. Hurtalová, E. Tillová, M. Chalupová, and J. Piatkowski, “Optical and scanning electron microscope studies of recycled (Secondary) Al-Si cast alloys,” *Solid State Phenom.*, vol. 203–204, no. June, pp. 266–271, 2013, doi: 10.4028/www.scientific.net/SSP.203-204.266.
- [2] Z. Hu, L. Wan, S. Lü, P. Zhu, and S. Wu, “Research on the microstructure, fatigue and corrosion behavior of permanent mold and die cast aluminum alloy,” *Mater. Des.*, vol. 55, pp. 353–360, 2014, doi: 10.1016/j.matdes.2013.10.012.
- [3] G. K. Sigworth and R. J. Donahue, “The Metallurgy of Aluminum Alloys for Structural High-Pressure Die Castings,” *Int. J. Met.*, vol. 15, no. 3, pp. 1031–1046, 2021, doi: 10.1007/s40962-020-00535-x.
- [4] M. Hartlieb, “The Market for Aluminum Alloys in North America: Trends & Challenges,” *Die Casting Engineer Magazine*, 2016.
- [5] L. Kuchariková, E. Tillová, and O. Bokůvka, “Recycling and properties of recycled aluminium alloys used in the transportation industry,” *Transp. Probl.*, vol. 11, no. 2, pp. 117–122, 2016, doi: 10.20858/tp.2016.11.2.11.
- [6] L. Fei, Z. Haidong, Y. Runsheng, and S. Fengzhen, “Microstructure and Mechanical Properties of High Vacuum Die-Cast AlSiMgMn Alloys at as-Cast and T6-Treated Conditions,” *Materials (Basel)*, vol. 12, no. 13, pp. 1–14, 2019.
- [7] S. Park, C. Ahn, and E. Lee, “Evaluation of corrosion behavior on crept als10mnmg (Aa365) alloy produced by high-pressure die-casting (hpdc),” *Appl. Sci.*, vol. 11, no. 13, 2021, doi: 10.3390/app11136227.

- [8] R. Arrabal, B. Mingo, A. Pardo, M. Mohedano, E. Matykina, and I. Rodríguez, “Pitting corrosion of rheocast A356 aluminium alloy in 3.5wt.% NaCl solution,” *Corros. Sci.*, vol. 73, pp. 342–355, 2013, doi: 10.1016/j.corsci.2013.04.023.
- [9] J. Kim, S. Shin, and S. Lee, “Correlation between microstructural evolution and corrosion resistance of hypoeutectic Al–Si–Mg alloy: Influence of corrosion product layer,” *Mater. Charact.*, vol. 193, no. September, p. 112276, 2022, doi: 10.1016/j.matchar.2022.112276.
- [10] D. Culliton, A. J. Betts, and D. Kennedy, “Impact of intermetallic precipitates on the tribological and/or corrosion performance of cast aluminium alloys: A short review,” *Int. J. Cast Met. Res.*, vol. 26, no. 2, pp. 65–71, 2013, doi: 10.1179/1743133612Y.0000000038.
- [11] J. O. Park, C. H. Paik, Y. H. Huang, and R. C. Alkire, “Influence of Fe-Rich Intermetallic Inclusions on Pit Initiation on Aluminum Alloys in Aerated NaCl,” *J. Electrochem. Soc.*, vol. 146, no. 2, pp. 517–523, 1999, doi: 10.1149/1.1391637.
- [12] S. Sainis, S. Roşoiu, E. Ghassemali, and C. Zanella, “Surface & Coatings Technology The role of microstructure and cathodic intermetallics in localised deposition mechanism of conversion compounds on Al (Si , Fe , Cu) alloy,” *Surf. Coat. Technol.*, vol. 402, no. July, p. 126502, 2020, doi: 10.1016/j.surfcoat.2020.126502.
- [13] D. Bösch *et al.*, “Secondary Al-Si-Mg High-pressure Die Casting Alloys with Enhanced Ductility,” *Metall. Mater. Trans. A Phys. Metall. Mater. Sci.*, vol. 46, no. 3, pp. 1035–1045, 2015, doi: 10.1007/s11661-014-2700-8.

- [14] R. Lumley, “The Development of High Strength and Ductility in High-Pressure Die-Cast Al-Si-Mg Alloys from Secondary Sources,” *Jom*, vol. 71, no. 1, pp. 382–390, 2019, doi: 10.1007/s11837-018-3121-8.
- [15] E. Cinkilic, M. Moodispaw, J. Zhang, J. Miao, and A. A. Luo, “A New Recycled Al–Si–Mg Alloy for Sustainable Structural Die Casting Applications,” *Metall. Mater. Trans. A Phys. Metall. Mater. Sci.*, vol. 53, no. 8, pp. 2861–2873, 2022, doi: 10.1007/s11661-022-06711-4.
- [16] D. Závodská, E. Tillová, I. Švecová, L. Kuchariková, and M. Chalupová, “Secondary cast Al-alloys with higher content of iron,” *Mater. Today Proc.*, vol. 5, no. 13, pp. 26680–26686, 2018, doi: 10.1016/j.matpr.2018.08.135.
- [17] L. Kuchariková, T. Liptáková, E. Tillová, D. Kajánek, and E. Schmidová, “Role of chemical composition in corrosion of aluminum alloys,” *Metals (Basel)*, vol. 8, no. 8, pp. 1–13, 2018, doi: 10.3390/met8080581.
- [18] S. Cecchel, G. Cornacchia, and M. Gelfi, “Corrosion behavior of primary and secondary AlSi high pressure die casting alloys,” *Mater. Corros.*, vol. 68, no. 9, pp. 961–969, 2017, doi: 10.1002/maco.201709526.
- [19] N. Yunusov, “Aluminium Primär-/Sekundärlegierungen,” 2021.
- [20] R. B. C. Cayless, “Alloy and Temper Designation Systems for Aluminum and Aluminum Alloys,” in *Nonferrous Alloys and Special-Purpose Materials*, vol. 2, ASM International, 1990, pp. 15–28.
- [21] J. G. Kaufman, “Understanding Wrought and Cast Aluminum Alloys Designations,” in *Introduction to Aluminium Alloys and Tempers*, 2000, pp. 23–37.

- [22] H. Xiaoxia, Y. Hua, Z. Yan, and P. Fuzhen, “Effect of Si on the interaction between die casting die and aluminum alloy,” *Mater. Lett.*, vol. 58, no. 27–28, pp. 3424–3427, 2004, doi: 10.1016/j.matlet.2004.06.021.
- [23] S. Wang, M. Fu, X. Li, J. Wang, and X. Su, “Microstructure and mechanical properties of Al–Si eutectic alloy modified with Al–3P master alloy,” *J. Mater. Process. Technol.*, vol. 255, no. August 2017, pp. 105–109, 2018, doi: 10.1016/j.jmatprotec.2017.12.008.
- [24] P. P. Seth, O. Parkash, and D. Kumar, “Structure and mechanical behavior of in situ developed Mg₂Si phase in magnesium and aluminum alloys - a review,” *RSC Adv.*, vol. 10, no. 61, pp. 37327–37345, 2020, doi: 10.1039/d0ra02744h.
- [25] Y. M. Kim, S. W. Choi, Y. C. Kim, C. S. Kang, and S. K. Hong, “The influence of the additional Fe and Mn in Al alloy on the die soldering phenomenon,” *J. Nanosci. Nanotechnol.*, vol. 16, no. 11, pp. 11252–11255, 2016, doi: 10.1166/jnn.2016.13488.
- [26] S. G. Shabestari, “The effect of iron and manganese on the formation of intermetallic compounds in aluminum–silicon alloys,” *Mater. Sci. Eng. A*, vol. 383, no. 2, pp. 289–298, Oct. 2004, doi: 10.1016/j.msea.2004.06.022.
- [27] G. K. Sigworth and T. A. Kuhn, “Grain refinement of aluminum casting alloys,” *Int. J. Met.*, vol. 1, no. 1, pp. 31–40, 2007, doi: 10.1007/BF03355416.
- [28] Q. Miao *et al.*, “Comparative study of microstructure evaluation and mechanical properties of 4043 aluminum alloy fabricated by wire-based additive manufacturing,” *Mater. Des.*, vol. 186, p. 108205, 2020, doi:

10.1016/j.matdes.2019.108205.

- [29] E. Lordan *et al.*, “High-Pressure Die Casting: A Review of Progress from the EPSRC Future LiME Hub,” *Metals (Basel)*., vol. 12, no. 10, 2022, doi: 10.3390/met12101575.
- [30] M. Liu, Z. Zhang, F. Breton, and X. G. Chen, “Investigation of the quench sensitivity of an AlSi10Mg alloy in permanent mold and high-pressure vacuum die castings,” *Materials (Basel)*., vol. 12, no. 11, 2019, doi: 10.3390/ma12111876.
- [31] X. P. Niu, B. H. Hu, I. Pinwill, and H. Li, “Vacuum assisted high pressure die casting of aluminium alloys,” *J. Mater. Process. Technol.*, vol. 105, no. 1–2, pp. 119–127, 2000, doi: 10.1016/S0924-0136(00)00545-8.
- [32] L. Wan, Z. Hu, S. Wu, and X. Liu, “Mechanical properties and fatigue behavior of vacuum-assist die cast AlMgSiMn alloy,” *Mater. Sci. Eng. A*, vol. 576, pp. 252–258, 2013, doi: 10.1016/j.msea.2013.03.042.
- [33] X. Dong, X. Zhu, and S. Ji, “Effect of super vacuum assisted high pressure die casting on the repeatability of mechanical properties of Al-Si-Mg-Mn die-cast alloys,” *J. Mater. Process. Technol.*, vol. 266, no. October 2018, pp. 105–113, 2019, doi: 10.1016/j.jmatprotec.2018.10.030.
- [34] W. D. Callister and D. G. Rethwisch, *Materials Science and Engineering: An Introduction*, 9th Editio. John Wiley & Sons, Inc., 2013.
- [35] C. D. Marioara, S. J. Andersen, J. Jansen, and H. W. Zandbergen, “Atomic model for GP-zones in a 6082 Al-Mg-Si system,” *Acta Mater.*, vol. 49, no. 2, pp. 321–328, 2001, doi: 10.1016/S1359-6454(00)00302-5.

- [36] R. X. Li *et al.*, “Age-hardening behavior of cast Al-Si base alloy,” *Mater. Lett.*, vol. 58, no. 15, pp. 2096–2101, 2004, doi: 10.1016/j.matlet.2003.12.027.
- [37] L. K. Berg *et al.*, “GP-zones in Al-Zn-Mg alloys and their role in artificial aging,” *Acta Mater.*, vol. 49, no. 17, pp. 3443–3451, 2001, doi: 10.1016/S1359-6454(01)00251-8.
- [38] G. B. Burger, A. K. Gupta, P. W. Jeffrey, and D. J. Lloyd, “Microstructural control of aluminum sheet used in automotive applications,” *Mater. Charact.*, vol. 35, no. 1, pp. 23–39, 1995, doi: 10.1016/1044-5803(95)00065-8.
- [39] A. M. A. Mohamed and F. H. Samuel, “A Review on the Heat Treatment of Al-Si-Cu/Mg Casting Alloys,” in *Heat Treatment - Conventional and Novel Applications*, 2012.
- [40] P. Ashtari, H. Tezuka, and T. Sato, “Influence of Sr and Mn additions on intermetallic compound morphologies in Al-Si-Cu-Fe cast alloys,” *Mater. Trans.*, vol. 44, no. 12, pp. 2611–2616, 2003, doi: 10.2320/matertrans.44.2611.
- [41] M. Shakiba, N. Parson, and X. G. Chen, “Effect of homogenization treatment and silicon content on the microstructure and hot workability of dilute Al-Fe-Si alloys,” *Mater. Sci. Eng. A*, vol. 619, no. December 2014, pp. 180–189, 2014, doi: 10.1016/j.msea.2014.09.072.
- [42] E. Cinkilic, C. D. Ridgeway, X. Yan, and A. A. Luo, “A Formation Map of Iron-Containing Intermetallic Phases in Recycled Cast Aluminum Alloys,” *Metall. Mater. Trans. A*, vol. 50, no. 12, pp. 5945–5956, 2019, doi: 10.1007/s11661-019-05469-6.

- [43] C. Bidmeshki, V. Abouei, H. Saghafian, S. G. Shabestari, and M. T. Noghani, “Effect of Mn addition on Fe-rich intermetallics morphology and dry sliding wear investigation of hypereutectic Al-17.5%Si alloys,” *J. Mater. Res. Technol.*, vol. 5, no. 3, pp. 250–258, 2016, doi: 10.1016/j.jmrt.2015.11.008.
- [44] M. Kohlhepp, P. J. Uggowitzer, M. Hummel, and H. W. Höppel, “Formation of die soldering and the influence of alloying elements on the intermetallic interface,” *Materials (Basel)*, vol. 14, no. 7, 2021, doi: 10.3390/ma14071580.
- [45] K. Yang, A. V. Nagasekhar, and C. H. Caceres, “The Skin Effect in High Pressure Die Casting Al Alloys,” no. The Japan Institute of Light Metals, pp. 687–692, 2010, doi: 10.4028/www.scientific.net/AMR.97-101.743.
- [46] Z. W. Chen, “Skin solidification during high pressure die casting of Al-11Si-2Cu-1Fe alloy,” *Mater. Sci. Eng. A*, vol. 348, no. 1–2, pp. 145–153, 2003, doi: 10.1016/S0921-5093(02)00747-5.
- [47] S. Esmailzadeh, M. Aliofkhazraei, and H. Sarlak, “Interpretation of Cyclic Potentiodynamic Polarization Test Results for Study of Corrosion Behavior of Metals: A Review,” *Prot. Met. Phys. Chem. Surfaces*, vol. 54, no. 5, pp. 976–989, 2018, doi: 10.1134/S207020511805026X.
- [48] S. B. Arya and F. J. Joseph, “Electrochemical methods in tribocorrosion,” in *Tribocorrosion Fundamentals, Methods, and Materials*, Elsevier Inc., 2021, pp. 43–77.
- [49] S. A. Fernández and M. G. Alvarez, “Passivity breakdown and stress corrosion cracking of α -brass in sodium nitrate solutions,” *Corros. Sci.*, vol. 53, no. 1, pp.

82–88, 2011, doi: 10.1016/j.corsci.2010.09.025.

- [50] A. A. Dastgerdi, A. Brenna, M. Ormellese, M. P. Pedferri, and F. Bolzoni, “Experimental design to study the influence of temperature, pH, and chloride concentration on the pitting and crevice corrosion of UNS S30403 stainless steel,” *Corros. Sci.*, vol. 159, no. August, p. 108160, 2019, doi: 10.1016/j.corsci.2019.108160.
- [51] J. R. Davis, “Aluminum and Aluminum Alloys,” *Alloy. Underst. Basics*, pp. 351–416, 2001, doi: 10.1361/autb2001p351.
- [52] J. Esquivel and R. K. Gupta, “Review—Corrosion-Resistant Metastable Al Alloys: An Overview of Corrosion Mechanisms,” *J. Electrochem. Soc.*, vol. 167, no. 8, p. 081504, 2020, doi: 10.1149/1945-7111/ab8a97.
- [53] R. Winston Revie and H. H. Uhlig, “Corrosion and Corrosion Control,” in *Wiley-Interscience*, 2008.
- [54] G. S. Frankel and T. Ohio, “(V13A)Pitting Corrosion,” vol. 13, pp. 236–241, 2003, doi: 10.31399/asm.hb.v13a.a0003612.
- [55] H. Parangusan, J. Bhadra, and N. Al-Thani, “A review of passivity breakdown on metal surfaces: influence of chloride- and sulfide-ion concentrations, temperature, and pH,” *Emergent Mater.*, vol. 4, no. 5, pp. 1187–1203, 2021, doi: 10.1007/s42247-021-00194-6.
- [56] T. . Hoar, M. D.C, and R. G.P, “THE RELATIONSHIPS BETWEEN ANODIC PASSIVITY, BRIGHTENING AND PITTING,” *Corros. Sci.*, vol. 5, p. 1965, 1965.

- [57] S. Ahn, H. S. Kwon, and D. D. Macdonald, “The role of chloride ion in passivity breakdown on nickel,” *Proc. - Electrochem. Soc.*, vol. PV 2004-19, pp. 237–247, 2006, doi: 10.1149/1.2048247.
- [58] D. D. MacDonald, “The history of the Point Defect Model for the passive state: A brief review of film growth aspects,” *Electrochim. Acta*, vol. 56, no. 4, pp. 1761–1772, 2011, doi: 10.1016/j.electacta.2010.11.005.
- [59] P. Fathi, M. Mohammadi, X. Duan, and A. M. Nasiri, “A comparative study on corrosion and microstructure of direct metal laser sintered AlSi10Mg_200C and die cast A360.1 aluminum,” *J. Mater. Process. Technol.*, vol. 259, no. October 2017, pp. 1–14, 2018, doi: 10.1016/j.jmatprotec.2018.04.013.
- [60] M. A. Pech-Canul, R. Giridharagopal, M. I. Pech-Canul, and E. E. Coral-Escobar, “Localized corrosion behavior of Al-Si-Mg alloys used for fabrication of aluminum matrix composites,” *J. Mater. Eng. Perform.*, vol. 22, no. 12, pp. 3922–3932, 2013, doi: 10.1007/s11665-013-0674-0.
- [61] K. Nisancioglu, “Electrochemical Behavior of Aluminum - Base Intermetallics Containing Iron,” *J. Electrochem. Soc.*, vol. 137, pp. 69–77, 1990.
- [62] M. Á. Castro-Sastre, C. García-Cabezón, A. I. Fernández-Abia, F. Martín-Pedrosa, and J. Barreiro, “Comparative study on microstructure and corrosion resistance of al-si alloy cast from sand mold and binder jetting mold,” *Metals (Basel)*, vol. 11, no. 9, pp. 1–16, 2021, doi: 10.3390/met11091421.
- [63] C. Berlanga *et al.*, “Evaluation of the corrosion resistance of a new AlSi10MnMg(Fe) secondary alloy,” *Mater. Today Proc.*, vol. 10, pp. 312–318,

- 2019, doi: 10.1016/j.matpr.2018.10.411.
- [64] N. Birbilis and R. G. Buchheit, “Electrochemical Characteristics of Intermetallic Phases in Aluminum Alloys,” *J. Electrochem. Soc.*, vol. 152, no. 4, p. B140, 2005, doi: 10.1149/1.1869984.
- [65] S. K. Das, “Designing aluminum alloys for a recycling friendly world,” *Mater. Sci. Forum*, vol. 519–521, no. PART 2, pp. 1239–1244, 2006, doi: 10.4028/www.scientific.net/MSF.519-521.1239.
- [66] R. Wieszala, J. Piątkowski, and J. Kozuba, “Influence of manganese on the microstructure of secondary alloys Al-Si-Mg,” *Met. 2019 - 28th Int. Conf. Metall. Mater. Conf. Proc.*, no. January, pp. 1230–1240, 2019, doi: 10.37904/metal.2019.769.
- [67] A. Niklas *et al.*, “A new secondary AlSi10MnMg(Fe) alloy suitable for manufacturing of ductile Aluminium parts by vacuum assisted high pressure die casting technology,” *Metall. Ital.*, vol. 108, no. 6, pp. 9–12, 2016.
- [68] K. Anderson, J. Weritz, and J. G. Kaufman, “365.0 (Silafont®-36) and A365.0 (Aural®-2/-3),” in *ASM Handbook, Properties and Selection of Aluminum Alloys*, vol. 2B, 2019, pp. 561–563.
- [69] A. Niklas, A. Bakedano, S. Orden, M. da Silva, E. Nogués, and A. I. Fernández-Calvo, *Effect of Microstructure and Casting Defects on the Mechanical Properties of Secondary AlSi10MnMg(Fe) Test Parts Manufactured by Vacuum Assisted high Pressure Die Casting Technology*, vol. 2, no. 10. Elsevier Ltd., 2015.
- [70] B. Suárez-Peña and J. Asensio-Lozano, “Influence of Sr modification and Ti grain

- refinement on the morphology of Fe-rich precipitates in eutectic Al–Si die cast alloys,” *Scr. Mater.*, vol. 54, no. 9, pp. 1543–1548, May 2006, doi: 10.1016/j.scriptamat.2006.01.029.
- [71] Y. Gui, X. B. Meng, Z. J. Zheng, and Y. Gao, “Critical temperature determination of detectable Cr diffusion enhancement by nanostructure through structural evolution analysis of the oxide films at 25–450 °C on 304 stainless steel,” *Appl. Surf. Sci.*, vol. 419, pp. 512–521, 2017, doi: 10.1016/j.apsusc.2017.04.133.
- [72] H. J. Mathieu and D. Landolt, “An investigation of thin oxide films thermally grown in situ on Fe₂₄Cr and Fe₂₄Cr₁₁Mo by auger electron spectroscopy and X-ray photoelectron spectroscopy,” *Corros. Sci.*, vol. 26, no. 7, pp. 547–559, 1986, doi: 10.1016/0010-938X(86)90022-3.
- [73] A. Pardo, M. C. Merino, F. Viejo, S. Feliú, M. Carboneras, and R. Arrabal, “Corrosion Behavior of Cast Aluminum Matrix Composites (A_{3xx}. xSiCp) in Chloride Media,” *J. Electrochem. Soc.*, vol. 152, no. 6, p. B198, 2005, doi: 10.1149/1.1899267.
- [74] A. Dobkowska, B. Adamczyk-Cieślak, J. Mizera, K. J. Kurzydłowski, and A. Kiełbus, “The comparison of the microstructure and corrosion resistance of sand cast aluminum alloys,” *Arch. Metall. Mater.*, vol. 61, no. 1, pp. 209–212, 2016, doi: 10.1515/amm-2016-0038.
- [75] W. R. Osório, C. M. Freire, and A. Garcia, “The role of macrostructural morphology and grain size on the corrosion resistance of Zn and Al castings,” *Mater. Sci. Eng. A*, vol. 402, no. 1–2, pp. 22–32, 2005, doi:

10.1016/j.msea.2005.02.094.

- [76] S. ono, G. Priyotomo, and L. Nuraini, “The Selection of Magnesium alloys as Sacrificial Anode for the Cathodic Protection of Underground Steel Structure,” *Int. J. Eng. Trends Technol.*, vol. 51, no. 2, pp. 78–82, 2017, doi: 10.14445/22315381/ijett-v51p214.
- [77] A. I. Ikeuba, B. Zhang, J. Wang, E.-H. Han, W. Ke, and P. C. Okafor, “SVET and SIET Study of Galvanic Corrosion of Al/MgZn 2 in Aqueous Solutions at Different pH,” *J. Electrochem. Soc.*, vol. 165, no. 3, pp. C180–C194, 2018, doi: 10.1149/2.0861803jes.
- [78] Y. T. Zhou, X. L. Jia, J. B. Li, G. G. Guan, X. L. Ma, and J. S. Zhang, “Unraveling the precipitate-induced discontinuity of the surface oxide film on Al alloy,” *Appl. Surf. Sci.*, vol. 590, no. November 2021, 2022, doi: 10.1016/j.apsusc.2022.153108.